THE JOURNAL OF PHYSICAL CHEMISTRY C
A JOURNAL OF THE AMERICAN CHEMICAL SOCIETY

Density Functional Theory Estimate of Halide Perovskite Band Gap: When Spin Orbit Coupling Helps

Tilak Das, Giovanni Di Liberto,* and Gianfranco Pacchioni

Cite This: *J. Phys. Chem. C* 2022, 126, 2184−2198 **Read Online**

ACCESS | Metrics & More | Article Recommendations | Supporting Information

ABSTRACT: The description of the band gap of halide perovskites at the level of density functional theory (DFT) has been subject of several studies but still presents significant problems and deviations from experimental values. Various approaches have been proposed, including the use of system-specific hybrid functionals with a variable amount of exact exchange or the explicit inclusion of spin−orbit coupling (SOC) effects. In this work, we present a pragmatic recipe to compute the band gap of halide perovskites with a minimum average error. The recipe is tested on a set of 36 halide perovskites of the type ABX_3 [A = Cs, methyl-ammonium (MA), and formamidinium (FA); B = Ge, Sn, and Pb; and X = Cl, Br, and I] for which experimental estimates of the band gap have been reported in the literature. Upon assessment of the accuracy of commonly used DFT functionals and the analysis of their performances based on error and statistical analysis, we suggest a strategy to compute band gaps in halide perovskites with a single functional. This is based on the use of the hybrid HSE06 functional where SOC is included exclusively for Pb-containing compounds. The results are rationalized in terms of the materials' chemical nature and are corroborated by the prediction of their expected efficiencies in solar cells. The calculated efficiencies from band gaps obtained with the proposed approach closely follow the experimental trend, demonstrating the importance of adopting a reliable but material-independent computational strategy to screen new halide perovskite materials for solar energy conversion.

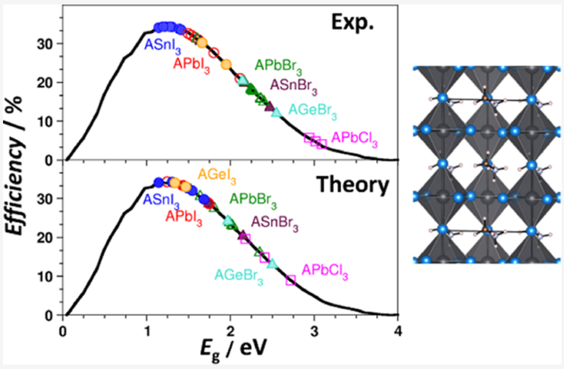

1. INTRODUCTION

The development of efficient devices capable of converting solar light into electrical or chemical energy in an efficient way is essential for the future of the energy transition. Starting from the pioneering work by Fujishima and Honda who demonstrated that a stable, cheap, and abundant material such as TiO_2 is active for the photocatalytic water splitting,[1] a lot of efforts have been devoted to the development of new materials for application in solar cells, photocatalysis, and environmental remediation.[2−6] Despite these efforts, very often single-phase materials display low efficiencies due to two detrimental events. The first issue is the band gap problem, which is typical of TiO_2 and ZnO to name a few and makes the material a poor light-absorbing species, thus resulting in an intrinsic low activity. The introduction of point defects that alter the electronic structure or nanostructuring that retains the chemical nature of the system has been considered a promising route to improve the absorption of visible light.[7−13] Unfortunately, a second problem is commonly present, due to the fast charge carrier recombination process. Indeed, upon visible light excitation, the generated electron−hole pairs must be separated and driven toward the active sites to produce electricity or chemical energy. However, electron−hole pairs are unstable, and the quickest relaxation process is their recombination. To solve this issue, composite materials have been considered, based on the capability to separate electrons and holes in different components of a heterojunction, thus hindering the recombination process.[4,14−17] In addition to the abovementioned problems, one should consider that the system must be stable under working conditions.[18−20]

Halide perovskites represent a promising class of compounds bearing many of the required properties as far as the conversion of solar light is concerned.[21−28] A perovskite is a solid with chemical formula ABX_3. Archetype of this type of crystal structures is $CaTiO_3$ or $SrTiO_3$. In halide perovskites, A is a monovalent cation, B is a divalent cation, and X is the halogen. B cations are octahedrally coordinated to X atoms and A cations occupy dodecahedral sites, formed by the network of corner-sharing octahedra. A can be either an inorganic species such as Cs^+ or organic as methyl ammonium (MA) and formamidinium (FA) ions. B is usually a cation of the fourth group Ge, Sn, or Pb. The halogen is commonly Cl, Br, or I.

Received: November 5, 2021
Revised: January 11, 2022
Published: January 24, 2022

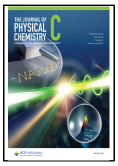

Halide perovskites are very versatile since the band gap can be tuned by modifying the chemical composition, and this allows one to obtain systems with the desired electronic properties. Such a strategy allows one to have materials with band gaps ranging from ~1.5 to ~3.0 eV.[25,26] The combination with other semiconductors such as TiO_2 helps in separating the electron and hole pairs; the oxide in the form of coating also acts as a protecting agent.[29−32] Fully inorganic halide perovskites showed higher stability when compared to their organic−inorganic analogues.[33]

Halide perovskites are widely applied in photocatalytic experiments and solar cells, showing in some cases very high power conversion efficiencies (PCEs).[34−37] Among others, Nasti and Abate reported recently a nice and detailed guide of Sn-based halide perovskite solar cells,[38] Guijarro et al. reported very high efficiency of organic lead halide perovskite solar cells,[39] and Manna and co-workers reported a seminal review of inorganic halide perovskites.[40]

The capability to tune the band gap of a semiconductor is a crucial aspect, since it has direct implications to the observed efficiency in the conversion of solar light. Shockley and Queisser showed that the maximum theoretical efficiency of a solar cell follows a mathematical relation with the band gap.[41] This result can be obtained by applying the concept of detailed balance. It was shown that the most efficient solar cells are those with a band gap around 1.1−1.2 eV, consistent with the experimental evidence.[42]

Given the versatility of halide perovskites in band gap tunability, electronic structure theory can be of great help when screening new potential materials with desired band gap values. The reliability of a calculation is strongly dependent on the accuracy that can be reached in the band gap estimation, since this has direct implications in the prediction of the efficiency in solar light conversion.

The band gap calculation of a material can be addressed by several approaches. Among the most accurate methods for the treatment of the excitation problem in a solid, one can find the GW approach,[43−45] which is in general computationally demanding.[46,47] The conventional computational methodology is based on density functional theory (DFT).[48−52] For the specific case of halide perovskites, several important studies have been reported.[52−54] DFT band gaps are obtained from the Kohn−Sham orbitals describing the conduction band maximum and conduction band minimum of a system, which of course represents an approximation of the real optical excitation problem, and excitonic effects are neglected.[55−60] It should be said that DFT provides a-thermal band gaps, therefore temperature effects are neglected. This aspect can be addressed by performing ab-initio molecular simulation at finite temperature,[61−63] and for this specific and challenging problem, we refer to a seminal work by Pasquarello and co-workers.[54] Despite the mentioned critical aspects, DFT represents a valid compromise between computational cost and accuracy.

Despite several efforts, the accurate description of the band gap of halide perovskites with a single formulation of the exchange−correlation functional in DFT is challenging and often results in relatively large errors. For this reason, it is common practice to study each perovskite with an ad hoc DFT hybrid functional specifically designed to reproduce the band gap of that specific perovskite.[64−69] Needless to say that this introduces a certain level of empiricism and severely limits the possibility to predict in a reliable way the properties and the band gap of an unknown perovskite, in the attempt to improve the results, it is common practice to include spin−orbit coupling (SOC) effects in the calculations.[46] However, we will show below that this is not always useful and it may result in worsening the agreement with the experiment. The exception is represented by the Pb-containing halide perovskites where the use of SOC is essential.

In this work, we propose a simple recipe for the calculation of the band gap of halide perovskites using a single DFT approach which results in an average accuracy in band gap prediction of 0.3 eV, which corresponds to an improvement of 0.2 eV compared to other commonly used approaches, and in a smaller standard deviation. To this end, we investigated at the DFT level, the entire set of perovskites of type ABX_3 (A = Cs, MA, or FA; B = Ge, Sn, or Pb; and X = Cl, Br, or I) for which both crystal structure and band gap are experimentally available. We have identified a set of 36 compounds for which these data exist.

The role of an accurate determination of the band gap for the prediction of the efficiency in solar energy conversion will be discussed. We will show that the proposed recipe allows one to provide sufficiently reliable efficiencies that closely follow the experimental trend, at variance with other conventional DFT functionals.

This work is organized as follows. We briefly summarize the computational details; then, we present the main results based on the working data set. In this section, we include an extensive list of experimentally determined band gap for halide perovskites with the known crystal structure. The results section includes the error analysis and a principal component analysis to rationalize the observed trends on a statistical basis. A subsection is dedicated to the calculation of the expected efficiencies in solar light conversion. Conclusions and future perspectives are summarized in the last section.

2. COMPUTATIONAL DETAILS

The calculations have been performed at the level of DFT as implemented in the VASP plane-wave-based code.[70−72] The projector augmented wave (PAW) pseudopotentials have been adopted.[73,74] The Perdew−Burke−Ernzerhof (PBE) and Heyd−Scuseria−Ernzerhof (HSE06) parametrizations of the exchange−correlation functional were used,[75,76] and dispersion contributions have been included by the Grimme's D3 scheme.[77] Spin−orbit coupling (SOC) effects were included through the noncollinear implementation either for the structural optimization and/or single-point runs.[78] Convergence in total energy was reached when the difference between two consecutive self-consistent electronic cycles was less than 1×10^{-8} eV, and the threshold for the convergence of the forces was set to 5 meV/Å. A working kinetic cutoff of 400 eV has been adopted. The choice of the *k*-point mesh was systematically tested to have converged values. 9 × 9 × 9 and 4 × 4 × 4 meshes were used for PBE and HSE06 calculations.

3. RESULTS AND DISCUSSION

3.1. Band Gap Data Set and Performances of DFT Functionals.

Before starting the analysis of calculated band gaps, we screened the literature with the aim of finding the experimentally available band gaps of ABX_3 perovskites (A = Cs, MA, or FA; B = Ge, Sn, or Pb; and X = Cl, Br, or I) in different polymorphic forms (α = cubic, γ = orthorhombic, and *t* = tetragonal). An example of the polymorphs' crystal structures is reported in Figure 1.

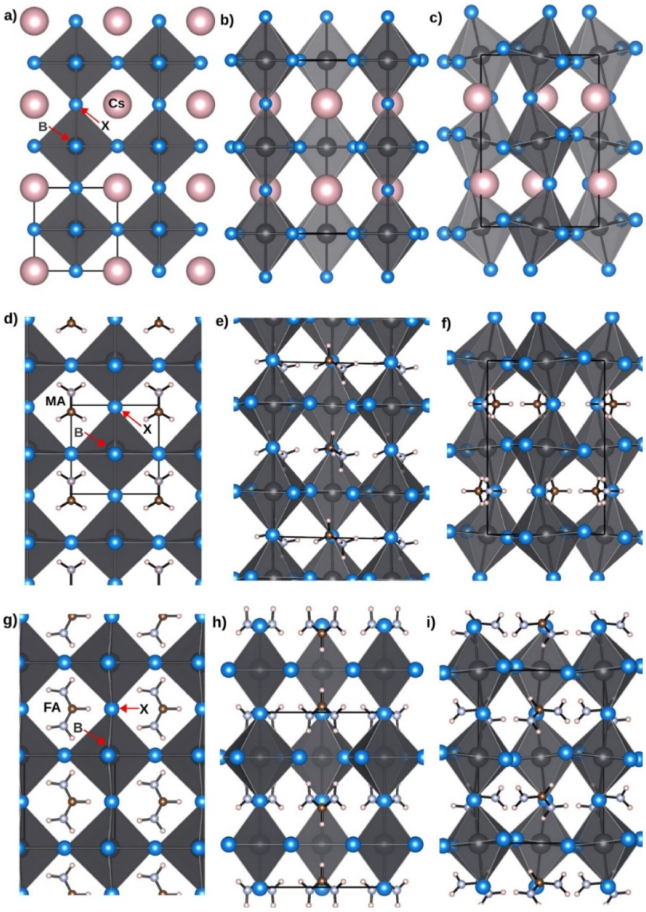

Figure 1. Example of the crystal structure of α-, γ-, and t-ABX_3 perovskites. Panels (a–c) are for $CsPbBr_3$, panels (d–f) are for $MAPbBr_3$, and panels (g–i) are for $FAPbBr_3$. Blue: Br; gray: Pb; pink: Cs; white: H; brown: C; and light blue: N.

Among the thousands of possible stable perovskites,[79] our data set has been chosen among the widely adopted ones for solar light-harvesting purposes in the halide family. As mentioned above, the crystal structure of the halide perovskites is similar in their cubic or noncubic phases, with corner-sharing BX_6 octahedra. The inorganic (or organic) cations are occupying the large dodecahedral sites in the unit cell, resulting from the network of octahedra. The impact of octahedral tilting and rotation of the organic cation has become matter of extensive research for the interpretation of the electronic band gap of halide perovskites.[80,81] They span from wide band gap semiconductors, for example, $APbCl_3$, to very low band gap ones such as $ASnI_3$. Table 1 reports a collection total of 127 experimentally determined values of band gaps of 36 perovskites, and Table S1 reports details of the perovskite crystal structures. In many cases, more than a single band gap value is available for the same material, the source of experimental gaps ranges from single crystals to powders to nanocrystals. For around 40% of the materials, single-crystal data are not available. Then, for the comparison with our calculations, we use the average of the reported experimental range of each species. Of course, this introduces some error bars on the values used to benchmark the DFT calculations. Among the full data set, the band gap values of α-$CsSnBr_3$ (1.36 eV) and α-$CsGeCl_3$ (2.03 eV) are quite off the mark from the other measurements. For this reason, they have not been included in the average. In Table 1, for each reported band gap, the experimental technique used is also reported.

As a first step, we fully optimized the bulk crystal structure of each perovskite at the PBE level and we evaluated the corresponding band gap, Table 2. The mean absolute error (MAE) from the experimental values is, not surprisingly, rather high, 0.65 eV, a common issue of GGA functionals. We repeated the band gap calculations using the experimental crystal structure, to estimate the contribution of lattice relaxation, which may be important when dealing with fluxional species. The absolute deviation remains high, 0.60 eV, showing that the crystal structure optimization has only a minor effect. Therefore, the rest of the calculations based on the HSE06 hybrid functional have been performed for the experimental crystal structures. Nevertheless, the absolute deviation of the computed band gaps moving from PBE (0.60 eV) to HSE06 (0.57 eV) remains unacceptably high, Table 2. Also, the standard deviation decreases by less than 0.1 eV, being 0.46 eV for PBE and 0.39 eV for HSE06.

One possible strategy to improve the description of a material consists into tuning the amount of exact Fock exchange. This choice is by definition material-dependent. For instance, one can tune the amount of exact Fock exchange to reproduce the experimental band gap of a material. Another theoretically more well-grounded approach is based on the self-consistent determination of the amount of Fock exchange based on the calculation of the dielectric constant.[82−86] This approach, named dielectric-dependent, in some cases results in good results but not always provides the expected overall improvement.[87] We tested the use of self-consistent dielectric dependent (DD) functionals for a subset of halide perovskites but this resulted in an overall deterioration of the band gaps estimates, with a net increase in the average error from 0.57 eV (HSE06) to 0.73 eV ($HSE06_{DD}$), Table S2. For this reason, the use of DD functionals has not been further investigated.

One important aspect that is usually neglected in DFT calculations is the contribution of SOC, which becomes important for heavy elements. The addition of SOC effects on HSE06 calculations has been shown to be effective in many examples, including perovskites.[169−171] Therefore, we repeated the band gap calculations at the HSE06/SOC level. SOC has a non-negligible effect on the band gaps, as expected. In all cases, the inclusion of SOC decreases the band gap. On average, the SOC contribution is around 1.0 eV for Pb-based perovskites, 0.35 eV for Sn-based ones, and it becomes 0.2 eV for Ge-based perovskites.

Quite surprisingly, despite the relevant SOC correction, the value of MAE at the HSE06/SOC level for the full set of perovskites considered becomes 0.43 eV and does show only a moderate improvement with respect to HSE06 (0.57 eV). Even worse, the situation when SOC is included at the PBE level, as here the MAE reaches the unacceptable value of 1.16 eV, Table 2.

Going in more detail, the HSE06 and HSE06/SOC performances are extremely dependent in a nontrivial way on the nature of the perovskite. MAE of HSE06 ranges from nearly zero for α-$MASnI_3$ and α-$MAGeBr_3$ to 1 eV for α-$CsSnCl_3$ and γ-$MAPbBr_3$. MAE of HSE06/SOC is almost zero for α-$FAPbI_3$ and *t*-$MASnI_3$, while it is more than 1 eV for α-$CsGeCl_3$ and $CsSnCl_3$. Also, the standard deviation of both

Table 1. Experimental Band Gaps of the ABX_3 Perovskites from the Literature[a]

N.	materials	band gap (type)	material types and measurement types (RT = room temperature)
1	α-$CsPbCl_3$	3.0 eV (direct)	thin film, band gap from combined ultraviolet (UV) photoemission, absorption and reflectivity spectra (30−90 K)[88]
		3.06 eV (direct)	thin films, band gap from UV−photoluminescence (PL)[26]
		3.18 eV (direct)	nanocrystals and bad gap from PL Spectra (RT)[89]
2	α-$CsPbBr_3$	2.3 eV (direct)	thin film, band gap from combined ultraviolet (UV) photoemission, absorption and reflectivity spectra (30−90 K)[90]
		2.35−2.40 eV (direct)	thin film 400−500 nm thick, band gap from reflection-corrected transmission spectra[91]
		2.32 eV (direct)	thin film 400−500 nm thick, band gap from absorption spectra and Tauc plot[91]
		2.43 eV (direct)	nanocrystals and PL spectra (RT)[89]
3	γ-$CsPbBr_3$	2.25 eV (direct)	single crystal, band gap from diffuse reflectance, photoluminescence and transmission spectra (RT)[92]
		2.29−2.33 eV (direct)	single crystal, excitonic band gap from temperature dependent PL spectra combined with transmission and absorbance spectra (10−180 K)[93]
		2.34 eV (direct)	powder crystal, band gap from UV−vis absorption and PL spectra[94]
		2.37 (direct)	143 nm thin film on Si substrate, band gap from optical absorption and ellipsometry measurement[95]
		2.48 eV (direct)	thin films, band gap from reflectance and transmittance spectra using UV−vis−NIR spectrophotometer (RT)[96]
		2.42−2.44 eV (direct)	nanocrystalline, band gap from spectroscopic ellipsometry and imaginary part of dielectric constant (77−400 K)[97]
4	α-$CsPbI_3$	1.73 eV (direct)	quantum dot films 3−13 nm thick, band gap from UV−vis absorption and PL spectra (333−458 K)[32]
		1.76 eV (direct)	nanocrystals, band gap from UV−vis and transient absorption spectra (328−367 K)[98]
		1.88 eV (direct)	nanocrystals and PL spectra (RT)[89]
		1.73 eV (direct)	crystalline thin film, band gap from UV−vis absorbance spectra combined with normalized PL spectra[99]
5	γ-$CsPbI_3$	1.72 eV (direct)	thin films, band gap from combined measurement with transmission, absorption and PL spectra (4−270 K)[100,101]
		1.63 eV (direct)	single crystal, band gap from optical absorption spectra[102]
		1.85 eV (direct)	thin films, band gap from reflectance and transmittance spectra using UV−vis−NIR spectrophotometer (77 K)[96]
		2.33−2.61 eV (direct)	powder crystal, optical band gap from Tauc plot on the UV−vis absorption spectra[103]
6	α-$CsSnCl_3$	2.9 eV (direct)	single crystal, band gap from luminescence spectra at 77 K temp.[104]
		2.8 eV (direct)	thin film, band gap from UV−vis−NIR absorption spectra (RT)[105]
7	α-$CsSnBr_3$	1.75 eV (direct)	thin film, band gap from UV−vis−NIR absorption spectra (RT)[105]
		1.36 eV (direct)	powder crystal, band gap from PL spectra measurement at room temp. (RT)[106]
		1.78 eV (direct)	150 nm thick thin films on FTO/TiO_2, optical band gap from absorption and Tauc-plot[107]
		1.92 eV (direct)	nanocrystals, band gap from optical absorption[108]
8	α-$CsSnI_3$	1.21−1.24 eV (direct)	thin films, band gap from temperature dependent PL at temp. 50−100 K[109]
9	γ-$CsSnI_3$	1.32 eV (direct)	polycrystalline thin film, band gap from PL spectra at temp. 300 K[110]
		1.30 eV (direct)	single crystal, band gap from diffuse reflectance and PL spectra at room temperature[111]
		1.31 eV (direct)	single crystal and also crystalline thin film on quartz, band gap from PL and Tauc-plot on the optical absorption spectra[112]
10	α-$CsGeCl_3$	3.67 eV (direct)	not mentioned[113]
		2.03 eV (direct)	nanorods, optical band gap from absorption and PL spectra (RT)[114]
		3.43 eV (direct)	powder crystal, band gap from UV−vis absorption spectra (RT)[115]
11	α-$CsGeBr_3$	2.32 eV (direct)	not mentioned[113]
		1.91 eV (direct)	nanorods, optical band gap from absorption and PL spectra (RT)[114]
		2.38 eV (direct)	powder crystal, band gap from UV−vis absorption spectra[115]
12	α-$CsGeI_3$	1.53 eV (direct)	not mentioned[113]
		1.80 eV (direct)	nanorods, optical band gap from absorption and PL spectra (RT)[114]
		1.63 eV (direct)	powder crystal, band gap from optical absorption and photoelectron spectra[116]
13	α-$MAPbCl_3$	2.97 eV (direct)	single crystal, band gap from combined ellipsometry and diffuse reflectance measurement (RT)[117]
		2.95 eV (direct)	single crystal and also thin film on SiO_2, band gap from UV−vis absorption spectra (RT)[118]
		2.88 eV (direct)	single crystal, band gap from absorption and PL spectra (RT)[119]
		3.02−3.15 eV (direct)	single crystal, band gap from temperature dependent optical absorption (RT)[120]
		3.05 eV (direct)	nanocrystals, band gap from PL Spectra (RT)[89]
		2.87−2.81 eV (direct)	single crystal, band gap from combined UV−vis and PL spectroscopy[121]
		3.1 eV (direct)	thin films from solid solution, band gap from solar spectrum emission curve combined with transmittance and absorption spectra[122]
14	α-$MAPbBr_3$	2.24 eV (direct)	single crystal, band gap from combined ellipsometry and diffuse reflectance measurement (RT)[117]
		2.3 eV (direct)	thin films from solid solution, band gap from solar spectrum emission curve combined with transmittance and absorption spectra[122]
		2.25 eV (direct)	single crystal and also thin film on SiO2, band gap from UV−vis absorption spectra (RT)[118]
		2.31 eV (direct)	crystalline thin film on silica, band gap from absorption and PL edge[123]
		2.22−2.35 eV (direct)	single crystal, band gap from diffuse reflectance andKubelka−Munk spectra[124]
		2.33 eV (direct)	nanocrystals and PL Spectra (RT)[89]

Table 1. continued

N.	materials	band gap (type)	material types and measurement types (RT = room temperature)
		2.30−2.33 eV (direct)	single crystal, band gap from temperature dependent spectroscopic ellipsometry and Tauc-plot on absorption spectra (183−440 K)[125]
15	γ-MAPbBr$_3$	2.29 eV (direct)	thin films, band gap from magneto optical absorption spectroscopy (140−200 K)[126]
		2.18−2.31 eV (direct)	single crystal, band gap from combined spectroscopic ellipsometry and PL spectra (77−295 K)[127]
16	α-MAPbI$_3$	1.69 eV (direct)	thin film on FTO, band gap from UV−vis optical absorption from temp. 310−400 K[128]
		1.55 eV (direct)	single crystal, band gap from combined ellipsometry and diffuse reflectance measurement (RT)[117]
		1.55 eV (direct)	single crystal and also thin film on SiO$_2$ of 400−500 nm thick, band gap from UV−vis absorption spectra (RT)[118]
		1.50 eV (direct)	single crystal, band gap from diffuse reflectance and Kubelka−Munk spectra (RT)[124]
		1.64 eV (direct)	nanocrystals, band gap from PL spectra (RT)[89]
17	t-MAPbI$_3$	1.55 eV (direct)	solid solution, band gap from electronic absorption spectra[129]
		1.57 eV (direct)	crystalline thin film, band gap from UV−vis absorbance spectra combined with normalized PL spectra[99]
		1.61−1.62 eV (direct)	polycrystalline sample, band gap from pressure induced PL spectra (RT)[130]
		1.60 eV (direct)	thin films, band gap from UV−vis spectroscopy[131]
		1.46 eV (direct)	single crystal from solid solution, band gap from combined PL and Tauc plot[132]
		1.52 eV (direct)	powder crystal, optical band gap fromTauc plot on the UV−vis absorption spectra (RT)[103]
18	γ-MAPbI$_3$	1.65 eV (direct)	thin film on FTO, band gap from UV−vis optical absorption at temp. 4.2 K[128]
		1.633 eV (direct)	single crystal, band gap from optical absorption spectra at temp. 77−296 K[133]
		1.51 eV (direct)	single crystal, band gap from diffuse reflectance and Kubelka−Munk spectra (RT)[134]
		1.59 eV (direct)	thin films, band gap from PL spectra at temp. 12−300 K[135]
19	α-MASnCl$_3$	3.69 eV (direct)	thin film on quartz, band gap from optical absorbance spectra[136]
		3.6 eV (direct)	not mentioned clearly[137]
20	α-MASnBr$_3$	2.2 eV (direct)	thin film, band gap from UV−vis optical band gap measurement[138]
		2.15 eV (direct)	thin film on quartz, band gap from optical absorbance spectra[136]
21	α-MASnI$_3$	1.2−1.4 eV (direct)	polycrystalline crystal, band gap from diffuse reflectance spectra and converted to optical absorbance according to Kubelka−Munk equation (RT)[139]
		1.3 eV (direct)	thin films, band gap from time resolved PL spectra[140]
		1.30 eV (direct)	solid solution, band gap from electronic absorption spectra[129]
		1.23 eV (direct)	powder crystal, optical band gap from absorption and PL spectra[141]
		1.41 eV (direct)	thin film deposited on mesoporous TiO$_2$ substrate, Tauc plot on the optical absorption spectra (RT)[142]
		1.15 eV (direct)	single crystal, band gap from UV−vis/NIR diffuse reflectance spectra under ambient condition (RT)[143]
22	t-MASnI$_3$	1.2 eV (direct)	single crystal, band gap from diffuse reflectance spectra and converted to optical absorbance (RT)[139]
		1.1 eV (direct)	solid solution thin film coated on porous TiO$_2$, band gap from electronic absorption spectra[144]
23	γ-MASnI$_3$	1.2 eV (direct)	spin-coated thin film on z-cut quartz crystal, band gap from temperature dependent PL and absorption measurement (8−295 K)[145]
24	α-MAGeBr$_3$	2.55 eV (direct)	powder crystal, band gap from absorption with Kubelka−Munk and PL Spectra (RT)[146]
25	α-MAGeI$_3$	1.90 eV (direct)	single crystal, band gap from absorption spectra[147]
		1.94 eV (direct)	solid solution, band gap from absorption and PL spectra[148]
		2.0 eV (direct)	powder crystal, band gap from optical absorption and photoelectron spectra (RT)[116]
		2.0 eV (direct)	thin film deposited on mesoporous TiO$_2$ substrate, Tauc plot on the optical absorption spectra (200 K)[142]
26	α-FAPbCl$_3$	3.00 eV (direct)	nanocrystals, band gap from PL spectra (RT)[89]
		2.89 eV (direct)	colloidal quantum dots, PL emission and absorption spectra[149]
		2.88 eV (direct)	powder bulk crystal, band gap from PL spectra[150]
27	α-FAPbBr$_3$	2.29 eV (direct)	nanocrystals, band gap from PL spectra (RT)[89]
		2.34 eV (direct)	colloidal quantum dots, PL emission and absorption spectra[149]
		2.21 eV (direct)	powder bulk crystal, band gap from PL Spectra[150]
		2.28−2.32 eV (direct)	single crystal, band gap from temperature dependent spectroscopic ellipsometry and Tauc plot on absorption spectra (183−440 K)[125]
		2.36 eV (direct)	cubic nanocrystals, band gap from transient absorption spectra (292−304 K)[151]
		2.27 eV (direct)	single crystals, pressure dependent band gap from in situ absorption and PL micrograph measurement (RT)[152]
		2.15 eV (direct)	single crystal, band gap from steady state absorption spectra combined with PL spectra (RT)[153]
28	t-FAPbBr$_3$	2.25−2.28 eV (direct)	single crystal, temperature dependent spectroscopic ellipsometry and Tauc plot (183−440 K)[125]
		2.29 eV (direct)	thin films, band gap from magneto optical absorption spectroscopy[126]
29	γ-FAPbBr$_3$	2.23 eV (direct)	thin films, band gap from magneto optical absorption spectroscopy (140−200 K)[126]
		2.10 eV (direct)	single crystals, pressure dependent band gap from in situ absorption and PL micrograph measurement (RT)[152]
30	α-FAPbI$_3$	1.54 eV (direct)	nanocrystals, band gap from PL spectra (RT)[89]
		1.59 eV (direct)	colloidal quantum dots, PL emission and absorption spectra (RT)[149]
		1.59 eV (direct)	nanocrystals, band gap from optical absorption and PL spectra[154]
		1.51 eV (direct)	powder bulk crystal, band gap from PL Spectra (RT)[150]
		1.48 eV (direct)	crystalline thin film, band gap from UV−vis absorbance spectra[99]

Table 1. continued

N.	materials	band gap (type)	material types and measurement types (RT = room temperature)
		1.47−1.50 eV (direct)	single crystal, band gap from spectroscopic ellipsometry (77−295 K)[155]
		1.41 eV (direct)	single crystal, band gap from steady state absorption spectra combined with PL spectra (RT)[153]
31	α-FASnBr$_3$	2.55 eV (direct)	powder crystal, band gap from diffuse reflectance (RT)[156]
		2.39 eV (direct)	powder crystal and possible mixture of cubic and orthorhombic phase, band gap from PL spectra vs. pressure (RT)[157]
32	α-FASnI$_3$	1.41 eV (direct)	polycrystalline crystal, band gap from diffuse reflectance spectra and converted to optical absorbance according to Kubelka−Munk equation (RT)[139]
		1.34−1.40 eV (direct)	spin-coated crystalline thin film, Tauc plot on the absorption edges and PL spectra combined band gap measurement (98 K-RT)[158]
		1.45 eV (direct)	crystalline 250 nm thick thin film, diffuse transmittance and reflectance spectra[159]
		1.4 eV (direct)	single crystal, band gap from UV−vis/NIR diffuse reflectance spectra under ambient condition (RT)[143]
33	t-FASnI$_3$	1.15−1.25 eV (direct)	single crystal, band gap from PL peak position (4 K-RT)[160]
34	γ-FASnI$_3$	1.4−1.41 eV (direct)	single crystal, band gap from diffuse reflectance spectra and converted to opticalabsorbance according to Kubelka−Munk equation (RT)[139]
		1.4 eV (direct)	thin films, band gap from absorption spectra[161]
		1.41 eV (direct)	thin films, band gap from Tauc plot on absorption spectra[162]
		1.44 eV (direct)	spin-coated thin film on ITO, band gap from Absorption spectra combined with steady-state PL and time-resolved PL decay[163]
35	t-CsPbBr$_3$	2.48−2.50 eV (direct)	nanocrystalline, band gap from spectroscopic ellipsometry and imaginary part of dielectric constant (77−400 K)[97]
		2.30 eV (direct)	single crystal, excitonic band gap from temperature dependent PL spectra (RT)[164]
36	t-MAPbBr$_3$	1.60−1.64 eV (direct)	thin film deposited on porous TiO$_2$, band gap from PL excitation spectra combined with transient absorption spectra[165]
		1.61 eV (direct)	thin film from thermal vapor deposition, band gap from optical transmittance and reflectance spectra[166]
		1.56−1.57 eV (direct)	single crystal, band gap from temperature-dependent PL spectra[167]
		1.58 eV (direct)	thin film on Si substrate, band gap from temperature-dependent PL spectra (10−300 K)[168]

[a] Each band gap value is accompanied by the corresponding experimental technique.

HSE06 and HSE06/SOC is almost the same, 0.39 and 0.34 eV, indicating that errors are sparse to a similar extent.

3.2. Principal Component Analysis. In order to rationalize the performances of the various functionals and to find the main correlations between the nature of the materials and calculated properties, we performed a principal component analysis (PCA).[172] PCA is a valuable methodology to unravel the most relevant correlations between different variables in a set of data. The methodology has been successfully applied in recent quantum chemical studies.[87,173,174] The variables describing a data set are transformed by applying a linear transformation. The new variables are called principal components (PCs) and their transformation coefficients are called loading vectors. A strong correlation/anticorrelation between two variables corresponds to almost parallel loading vectors forming an angle of 0°/180°, while orthogonal or nearly orthogonal vectors indicate the absence of any significant correlation between the variables.

The analysis has been performed by means of the R code.[175] In Figure 2, we report the so-called loading plot, where the original variables are reported in the new reference frame defined by the two most relevant PCs (PC1 and PC2), which is sufficient to describe 70% of the total variance of the system. In general, this is sufficient to neglect the contribution of the remaining components.[174]

The variables included in the analysis are the experimental gap (E_g^{exp}), the band gap obtained at the HSE06 (E_g^{HSE06}) and HSE06/SOC ($E_g^{HSE06/SOC}$) levels, the absolute deviation of HSE06 (ΔE_g^{HSE06}) and HSE06/SOC ($\Delta E_g^{HSE06/SOC}$) band gaps from the experiment, and the extent of the SOC correction (SOC). Moreover, we included in the analysis the atomic/molecular weight of the components A (M_A), B (M_B), and X (M_X) of ABX$_3$ perovskites. We assign an index describing whether the perovskite is cubic (cubic) or not. The reliability of the analysis has been checked by adding a few control cases, namely, variables whose reciprocal correlation is known. We have added three variables describing if the perovskites contain iodine, ($\mathrm{I_{con}}$), lead ($\mathrm{Pb_{con}}$), and if they are inorganic/organic ($\mathrm{Cs_{con}}$). Clearly, these three variables are expected to strongly correlate with the weights of X, B, and A, respectively. Finally, we added an additional control variable defined by the volume per formula unit (V_{fu}) that should correlate with the halogen size.

Among all variables, $\mathrm{Cs_{con}}$ and M_A, and the symmetry of the system are poorly described by the PCs, that is, they are not relevant in determining the correlations. This can be understood by the fact that while the nature of A has an effect both on the geometrical and electronic structure of ABX$_3$,[170,176] this is smaller than that of B and X. For this reason, they are not reported in Figure 2. The same plot containing all variables can be found in Figure S2. We first observe from Figure 2 that, as expected, the variable indicating the presence of iodine strongly correlates with the halogen weight. A similar result is found for the two variables $\mathrm{Pb_{con}}$ and M_B. In addition, V_{fu} and M_X strongly correlate as expected: the heavier is the halogen, the bigger is the unit cell. Both correlations demonstrate the reliability of the analysis.

Moving to the nontrivial correlations, SOC and M_B almost perfectly anticorrelate (angle equal to 180°). In fact, the heavier the B, the more intense and with a negative sign is the SOC correction. For Ge compounds, this is equal to −0.20 eV, for Sn −0.35 eV and for Pb −1.05 eV. Interestingly, SOC does not correlate with the nature of the halogen (angle 90°). The band gap error with HSE06 strongly correlates with the nature of cation B (angle 16°). Therefore, the lighter the B, the more accurate is the HSE06. Indeed, ΔE_g^{HSE06} is 0.29, 0.37, and 0.78

Table 2. Calculated Band Gaps (in eV) of ABX_3 Perovskites Investigated in This Work Using Various Approaches[a]

	material	PBE	PBE^{opt}	PBE/SOC	HSE06	HSE06/SOC	$Exp.^{av}$
1	α-$CsPbCl_3$	2.32	2.4	1.33	3.23	2.18	3.09
2	α-$CsPbBr_3$	1.9	2.1	1.05	2.71	1.64	2.36
3	γ-$CsPbBr_3$	1.81	2.06	0.81	3.07	2.03	2.37
4	α-$CsPbI_3$	1.75	1.74	0.87	2.39	1.25	1.81
5	γ-$CsPbI_3$	1.65	1.79	0.69	2.78	1.75	2.12
6	α-$CsSnCl_3$	1.19	1.3	0.97	1.78	1.42	2.85
7	α-$CsSnBr_3$	1.03	1.04	0.85	1.45	1.09	1.84
8	α-$CsSnI_3$	0.95	0.91	0.77	1.15	0.82	1.23
9	γ-$CsSnI_3$	0.55	0.69	0.23	1.49	1.13	1.31
10	α-$CsGeCl_3$	1.71	1.43	1.69	2.59	2.46	3.55
11	α-$CsGeBr_3$	1.35	1.19	1.25	1.97	1.79	2.15
12	α-$CsGeI_3$	1.2	1.12	1.05	1.61	1.34	1.67
13	α-$MAPbCl_3$	2.47	2.56	1.47	3.52	2.41	3.02
14	α-$MAPbBr_3$	2.05	2.04	1.12	2.93	1.81	2.28
15	γ-$MAPbBr_3$	1.99	2.15	1.10	3.28	2.35	2.25
16	α-$MAPbI_3$	1.77	1.65	0.87	2.50	1.32	1.62
17	t-$MAPbI_3$	1.45	1.44	0.43	2.55	1.45	1.54
18	γ-$MAPbI_3$	1.59	1.7	0.69	2.74	1.74	1.58
19	α-$MASnCl_3$	1.71	1.55	1.42	2.60	2.25	3.65
20	α-$MASnBr_3$	1.19	0.97	0.96	1.75	1.4	2.18
21	α-$MASnI_3$	0.97	0.77	0.78	1.31	0.92	1.28
22	t-$MASnI_3$	0.55	0.38	0.23	1.49	1.11	1.15
23	γ-$MASnI_3$	0.71	0.63	0.45	1.69	1.38	1.20
24	α-$MAGeBr_3$	1.64	1.27	1.11	2.5	2.32	2.55
25	α-$MAGeI_3$	1.24	1.04	1.07	1.73	1.47	1.95
26	α-$FAPbCl_3$	2.54	2.36	1.58	3.72	2.72	2.94
27	α-$FAPbBr_3$	2.05	1.94	1.13	3.03	2.02	2.26
28	t-$FAPbBr_3$	1.83	1.67	0.84	3.1	2.03	2.27
29	γ-$FAPbBr_3$	1.81	1.97	0.83	3.06	1.99	2.17
30	α-$FAPbI_3$	1.70	1.63	0.78	2.53	1.43	1.50
31	α-$FASnBr_3$	1.35	1.07	1.09	2.15	1.88	2.47
32	α-$FASnI_3$	0.99	0.87	0.75	1.50	1.17	1.40
33	t-FASnI3	0.57	0.33	0.29	1.49	1.13	1.20
34	γ-$FASnI_3$	0.61	0.47	0.29	1.55	1.19	1.42
35	t-$CsPbBr_3$	1.84	1.83	0.82	3.09	2.05	2.40
36	t-$MAPbBr_3$	1.75	1.89	0.73	2.99	2.07	1.60
MAE		**0.60**	**0.65**	**1.16**	**0.57**	**0.43**	
MUE		**−0.57**	**−0.62**	**−1.16**	**0.30**	**−0.38**	

[a] PBE band gaps at the optimized geometry are labeled PBE^{opt}. PBE, HSE06, and HSE06/SOC band gaps are calculated at the experimental crystal structure. The MAE and mean unsigned error (MUE) from the experimental values are reported in the last rows.

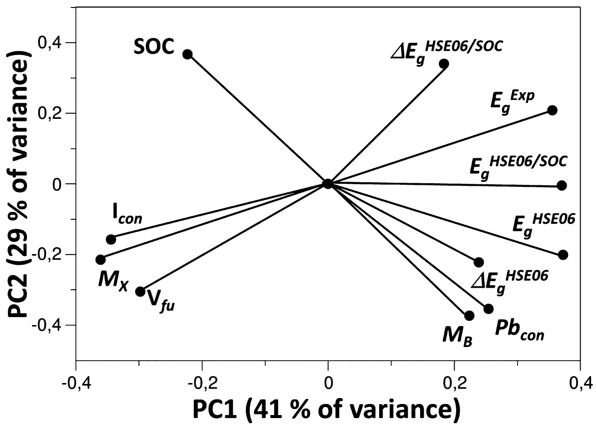

Figure 2. Loading plot made by the main PCs (PC1 and PC2). The original variables are reported as vectors in the new reference frame. For definition of the variables, see text.

eV for Ge-, Sn-, and Pb-containing compounds. This confirms that HSE06 performs well for Pb-free compounds. On the other hand, the nature of the halogen has a secondary role since a poor correlation (angle 106°) is observed with ΔE_g^{HSE06}.

The angle between M_B and ΔE_g increases from 16 to 121° when moving from HSE06 to HSE06/SOC, indicating that the error is less sensitive to the size of B; therefore, gap estimates of Pb-based compounds are more accurate. Indeed, $\Delta E_g^{HSE06/SOC}$ is rather stable when B varies: 0.50 eV (B = Ge), 0.51 eV (B = Sn), and 0.35 eV (B = Pb). On the contrary, a clear anticorrelation (angle = 150°) emerges between $\Delta E_g^{HSE06/SOC}$ and the nature of the halogen. In particular, MAE at the HSE06/SOC level goes from 0.94 eV for Cl-containing perovskites to 0.40 eV for Br- and to 0.25 eV for I-based compounds.

The results confirm that HSE06 and HSE06/SOC approaches work reasonably well for two different domains; (i) HSE06 estimates are reliable for all perovskites except for

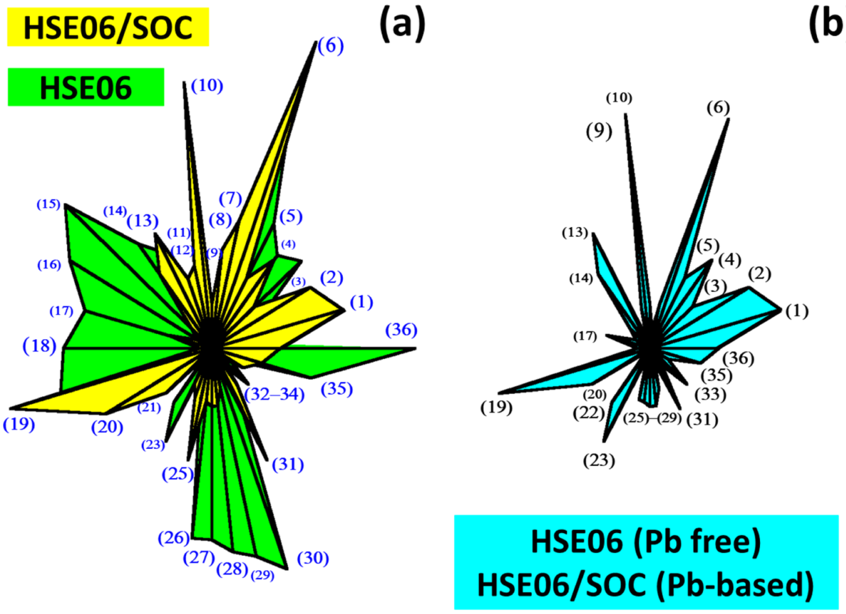

Figure 3. (a) Performances of the HSE06 functional with and without SOC in evaluating the band gap of the 36 halide perovskites. The numbers refer to the compounds reported in Tables 1 and 2. The length of each segment is proportional to the absolute deviation of the computed band gap from the experimental one. Yellow and green areas highlight the regions where HSE06/SOC and HSE06 show the highest deviations. (b) Same deviations using the approach proposed in this work.

those containing Pb, irrespective of the nature of the halogen; (ii) the use of SOC is recommended for Pb-based compounds, while it deteriorates the estimate of the band gap in the other cases, overcorrecting it. These conclusions explain the overall similar accuracy of HSE06 (MAE = 0.56 eV) and HSE06/SOC (MAE = 0.42 eV) over the entire data set.

According to this finding, with the proposed approach, MAE at the HSE06 level for Pb-free compounds decreases to 0.34 eV; at the same time, using the HSE06/SOC approach on Pb-containing perovskites, we obtain a very similar MAE, 0.35 eV. In both cases, the error is significantly decreased with respect to the case where the same approach, HSE06 or HSE06/SOC, is applied to the entire set. In addition, the standard deviation decreases as well to 0.29 eV by applying the SOC correction only to the Pb-containing compounds.

This conclusion can be better appreciated by looking at the graph reported in Figure 3. Each perovskite is defined by a vector in the plane. The length of each vector is proportional to the absolute deviation of the computed gap from the experimental one. For Pb-free compounds, the HSE06/SOC graph dominates over the HSE06 one because of the higher deviations (longer vectors), Figure 3a. On the contrary, for Pb-containing compounds, an opposite picture is obtained. By combining this information, one can construct the graph of Figure 3b where the HSE06 and HSE06/SOC estimates are used for the two separate set of perovskites, Pb-free ABX_3 and Pb-based ABX_3, respectively.

To summarize, with the statistical analysis, we have shown that it is possible to improve the estimate of the band gap of halide perovskites whose band gap is predicted with an average error of ∼0.3 eV using a single formulation of the exchange−correlation functional (HSE06) but including the spin−orbit correction only for the specific case where the B cation is Pb. This approach allows one to avoid the use of material-dependent functionals with different amounts of Fock exchange. A conclusive explanation of (i) the reason behind the error of HSE06 and HSE06/SOC approaches and (ii) why SOC tends to correct the band gap estimation for Pb-based compounds while it provides an overcorrection to Sn and Ge compounds is rather complex. A possible reason may be a combination of different factors, the first is related to the absence of temperature effects, as already mentioned; the second may be appointed to the complex and fluxional structure of some halide perovskites. An additional contribution may arise from the intrinsic error of DFT at the level of HSE06 and HSE06/SOC. Insights on the first two aspects could be obtained by performing dynamic simulations[54] and on the third aspect by adopting more elaborated methodologies for the electronic structure description as GW.

3.3. Band Gap and Expected Efficiency of Perovskite Solar Cells. The importance of the accurate prediction of band gaps for the screening of new materials is obvious but it can be better visualized by investigating the impact of band gap estimation on the predicted efficiency of halide perovskite solar cells. In fact, the band gap of a perovskite is directly related to the final efficiency of a solar cell.[42] One can evaluate the efficiency of a solar cell by integrating the fraction of solar power that can be absorbed by a perovskite.[177] This defines the so-called ultimate efficiency, which is the highest efficiency by neglecting any detrimental event. Of course, this is an upper bound and real efficiencies are lower. On the other hand, one can invoke the detailed balance approach pioneered by Shockley−Queisser,[41] which allows u to obtain PCEs quite close to the real ones.

Figure 4 reports the efficiency of halide perovskites as a function of their band gap according to the Shockley−Queisser formulation. Panel (a) shows the efficiency according to the experimental band gaps. The most efficient materials are $ASnI_3$ and $APbI_3$, since their band gap is close to the optimal one (∼1.1 eV). Then, $AGeI_3$, $APbBr_3$, $ASnBr_3$, and $AGeBr_3$ have a lower efficiency due to their higher gap. Among low-efficient perovskites is $APbCl_3$ with a predicted efficiency which is about one-fourth of the optimal one.

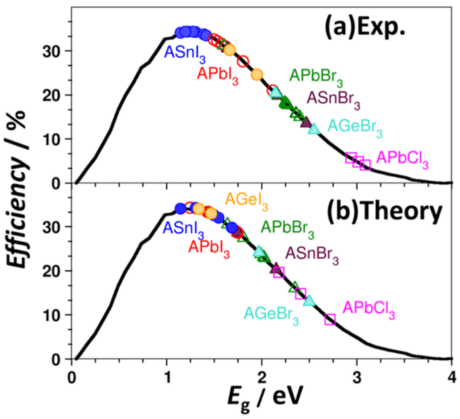

Figure 4. (a) Efficiency of 36 halide perovskites based on the experimental band gaps; (b) ultimate efficiency of 36 halide perovskites as obtained from the predicted band gaps according to the present approach. Circles: iodides; triangles: bromides; squares: chlorides; empty contour: Pb-based materials; solid contour: Sn-based materials; and dotted contour: Ge-based materials.

Interestingly, if we now estimate the efficiency using the computed band gaps following our proposed recipe, we retrieve a very similar trend, Figure 4b. On the contrary, if we use the HSE06 and HSE06-SOC band gaps for the full set of materials, we find significant deviations from Figure 4a (see Figure S3). In particular, the efficiency of APbBr$_3$ and APbI$_3$ perovskites is significantly lower (by 15−20%) when the HSE06 functional is used, while that of ASnBr$_3$ and ASnI$_3$ deviates from the experimental one due to the band gap overcorrection when HSE06/SOC is adopted, see Figure S3.

Thus, the experimental trend of efficiencies of halide perovskites cannot be reproduced using the HSE06 or HSE06/SOC approaches to compute the band gap for the entire set of materials, while a much better estimate is obtained by restricting the SOC correction to Pb-containing perovskites. The existence of a direct relationship between band gap and efficiency in solar light capture, although approximate, combined with the present recipe for the DFT estimate of the band gap, provides a powerful tool for the screening of new halide perovskites.

4. CONCLUSIONS

In this work, we proposed a simple recipe to evaluate the band gap of halide perovskites within the DFT approach. We selected a data set of 36 halide perovskites used in solar energy conversion experiments, for which both crystal structure and measured band gap are available from the literature. We listed a total of 127 band gap estimates for the 36 materials. This provides a solid database to benchmark the DFT-computed band gaps. Based on an error analysis, we found that the addition ofSOC to band gaps computed at the PBE level overcorrects the gaps and induces an overall deterioration of the accuracy. The addition of SOC to HSE06 for the entire set of perovskites does not result in a general increase in accuracy: while for some compounds, there is an improvement, for others, the results are clearly worse than at the HSE06 level. Based on a statistical analysis, we observed that the overall similar (and low) accuracy of HSE06 and HSE06/SOC when applied to the whole set of compounds is due to cancellation effects and that the two functionals work well under two different domains. In particular, HSE06 is valid for Pb-free compounds, while the use of HSE06/SOC is relevant for Pb-based perovskites.

Starting from this consideration, if we repeat the analysis of the average accuracy for the two separate set of materials, Pb-free or Pb-based, we found a significant increase in the accuracy and a decrease in the standard deviation. The implications of an improved accuracy in the estimate of the band gap were shown for the prediction of the PCE of halide perovskites. The proposed recipe allows us to retrieve the correct experimental trend of efficiencies, while using the HSE06 or HSE06/SOC for the entire set of data results in much worse agreement. It should also be mentioned that in this work, we looked at band gap estimation, but SOC may have a different impact on other important properties such as effective mass and optical absorption.

This simple strategy can be useful for the screening of the band gap of new halide perovskites and possible other materials for solar light-harvesting and has the clear advantage that does not require to select a specific material-dependent functional for the study of each system, thus increasing considerably the predictive power of DFT for this kind of problems.

■ ASSOCIATED CONTENT

Supporting Information

The Supporting Information is available free of charge at https://pubs.acs.org/doi/10.1021/acs.jpcc.1c09594.

Crystal structure information of the materials studied, self-consistent dielectric-dependent band gaps, and additional figures and tables related to band gap error and efficiency analysis (PDF)

■ AUTHOR INFORMATION

Corresponding Author

Giovanni Di Liberto − *Dipartimento di Scienza dei Materiali, Università degli Studi Milano-Bicocca, 20125 Milano, Italy*; orcid.org/0000-0003-4289-2732;
Email: giovanni.diliberto@unimib.it

Authors

Tilak Das − *Dipartimento di Scienza dei Materiali, Università degli Studi Milano-Bicocca, 20125 Milano, Italy*; orcid.org/0000-0002-9593-7888
Gianfranco Pacchioni − *Dipartimento di Scienza dei Materiali, Università degli Studi Milano-Bicocca, 20125 Milano, Italy*; orcid.org/0000-0002-4749-0751

Complete contact information is available at:
https://pubs.acs.org/10.1021/acs.jpcc.1c09594

Notes

The authors declare no competing financial interest.

■ ACKNOWLEDGMENTS

Financial support from the Italian Ministry of University and Research (MIUR) through PRIN Project 20179337R7 MULTI-e "Multielectron transfer for the conversion of small molecules: an enabling technology for the chemical use of renewable energy" and the grant Dipartimenti di Eccellenza—2017 "Materials For Energy" is gratefully acknowledged. We acknowledge CINECA under the ISCRAB initiatives for the availability of high-performance computing resources and support. We also thank the COST Action 18234 supported by European Cooperation in Science and Technology (COST).

■ REFERENCES

(1) Fujishima, A.; Honda, K. Electrochemical Photolysis of Water at a Semiconductor Electrode. *Nature* **1972**, *238*, 37−38.

(2) O'Regan, B.; Grätzel, M. A low-cost, high-efficiency solar cell based on dye-sensitized colloidal TiO2 films. *Nature* **1991**, *353*, 737−740.

(3) Hoffmann, M. R.; Martin, S. T.; Choi, W.; Bahnemann, D. W. Environmental Applications of Semiconductor Photocatalysis. *Chem. Rev.* **1995**, *95*, 69−96.

(4) Moniz, S. J. A.; Shevlin, S. A.; Martin, D. J.; Guo, Z.-X.; Tang, J. Visible-light driven heterojunction photocatalysts for water splitting - a critical review. *Energy Environ. Sci.* **2015**, *8*, 731−759.

(5) Linsebigler, A. L.; Lu, G.; Yates, J. T. Photocatalysis on TiO2 Surfaces: Principles, Mechanisms, and Selected Results. *Chem. Rev.* **1995**, *95*, 735−758.

(6) Schultz, D. M.; Yoon, T. P. Solar Synthesis: Prospects in Visible Light Photocatalysis. *Science* **2014**, *343*, 1239176.

(7) Livraghi, S.; Paganini, M. C.; Giamello, E.; Selloni, A.; Di Valentin, C.; Pacchioni, G. Origin of Photoactivity of Nitrogen-Doped Titanium Dioxide under Visible Light. *J. Am. Chem. Soc.* **2006**, *128*, 15666−15671.

(8) Di Valentin, C.; Finazzi, E.; Pacchioni, G.; Selloni, A.; Livraghi, S.; Paganini, M. C.; Giamello, E. N-Doped TiO2: Theory and Experiment. *Chem. Phys.* **2007**, *339*, 44−56.

(9) Tosoni, S.; Lamiel-Garcia, O.; Fernandez Hevia, D.; Doña, J. M.; Illas, F. Electronic Structure of F-Doped Bulk Rutile, Anatase, and Brookite Polymorphs of TiO2. *J. Phys. Chem. C* **2012**, *116*, 12738−12746.

(10) Marchiori, C.; Di Liberto, G.; Soliveri, G.; Loconte, L.; Lo Presti, L.; Meroni, D.; Ceotto, M.; Oliva, C.; Cappelli, S.; Cappelletti, G.; et al. Unraveling the Cooperative Mechanism of Visible-Light Absorption in Bulk N,Nb Codoped TiO2 Powders of Nanomaterials. *J. Phys. Chem. C* **2014**, *118*, 24152−24164.

(11) Rimoldi, L.; Ambrosi, C.; Di Liberto, G.; Lo Presti, L.; Ceotto, M.; Oliva, C.; Meroni, D.; Cappelli, S.; Cappelletti, G.; Soliveri, G.; et al. Impregnation versus Bulk Synthesis: How the Synthetic Route Affects the Photocatalytic Efficiency of Nb/Ta:N Codoped TiO2 Nanomaterials. *J. Phys. Chem. C* **2015**, *119*, 24104−24115.

(12) Morgan, B. J.; Scanlon, D. O.; Watson, G. W. Small Polarons in Nb- and Ta-Doped Rutile and Anatase TiO2. *J. Mater. Chem.* **2009**, *19*, 5175.

(13) Steveson, M.; Bredow, T.; Gerson, A. R. MSINDO Quantum Chemical Modelling Study of the Structure of Aluminium-Doped Anatase and Rutile Titanium Dioxide. *Phys. Chem. Chem. Phys.* **2002**, *4*, 358−365.

(14) Hurum, D. C.; Agrios, A. G.; Gray, K. A.; Rajh, T.; Thurnauer, M. C. Explaining the Enhanced Photocatalytic Activity of Degussa P25 Mixed-Phase TiO2 Using EPR. *J. Phys. Chem. B* **2003**, *107*, 4545−4549.

(15) Wang, H.; Zhang, L.; Chen, Z.; Hu, J.; Li, S.; Wang, Z.; Liu, J.; Wang, X. Semiconductor Heterojunction Photocatalysts: Design, Construction, and Photocatalytic Performances. *Chem. Soc. Rev.* **2014**, *43*, 5234.

(16) Low, J.; Yu, J.; Jaroniec, M.; Wageh, S.; Al-Ghamdi, A. A. Heterojunction Photocatalysts. *Adv. Mater.* **2017**, *29*, 1601694.

(17) Ko, K. C.; Bromley, S. T.; Lee, J. Y.; Illas, F. Size-Dependent Level Alignment between Rutile and Anatase TiO2 Nanoparticles: Implications for Photocatalysis. *J. Phys. Chem. Lett.* **2017**, *8*, 5593−5598.

(18) Li, P.; Sui, X.; Xu, J.; Jing, H.; Wu, C.; Peng, H.; Lu, J.; Yin, H. Worm-like InP/TiO2 NTs Heterojunction with Unmatched Energy Band Photo-Enhanced Electrocatalytic Reduction of CO2 to Methanol. *Chem. Eng. J.* **2014**, *247*, 25−32.

(19) Qiu, J.; Zeng, G.; Ha, M.-A.; Ge, M.; Lin, Y.; Hettick, M.; Hou, B.; Alexandrova, A. N.; Javey, A.; Cronin, S. B. Artificial Photosynthesis on TiO2-Passivated InP Nanopillars. *Nano Lett.* **2015**, *15*, 6177−6181.

(20) Zeng, G.; Qiu, J.; Hou, B.; Shi, H.; Lin, Y.; Hettick, M.; Javey, A.; Cronin, S. B. Enhanced Photocatalytic Reduction of CO2to CO through TiO2Passivation of InP in Ionic Liquids. *Chem.—Eur. J.* **2015**, *21*, 13502−13507.

(21) Xue, J.; Wang, R.; Yang, Y. The Surface of Halide Perovskites from Nano to Bulk. *Nat. Rev. Mater.* **2020**, *5*, 809−827.

(22) Grancini, G.; Roldán-Carmona, C.; Zimmermann, I.; Mosconi, E.; Lee, X.; Martineau, D.; Narbey, S.; Oswald, F.; De Angelis, F.; Graetzel, M.; et al. One-Year Stable Perovskite Solar Cells by 2D/3D Interface Engineering. *Nat. Commun.* **2017**, *8*, 15684.

(23) Akkerman, Q. A.; Motti, S. G.; Srimath Kandada, A. R.; Mosconi, E.; D'Innocenzo, V.; Bertoni, G.; Marras, S.; Kamino, B. A.; Miranda, L.; De Angelis, F.; et al. Solution Synthesis Approach to Colloidal Cesium Lead Halide Perovskite Nanoplatelets with Monolayer-Level Thickness Control. *J. Am. Chem. Soc.* **2016**, *138*, 1010−1016.

(24) Akkerman, Q. A.; D'Innocenzo, V.; Accornero, S.; Scarpellini, A.; Petrozza, A.; Prato, M.; Manna, L. Tuning the Optical Properties of Cesium Lead Halide Perovskite Nanocrystals by Anion Exchange Reactions. *J. Am. Chem. Soc.* **2015**, *137*, 10276−10281.

(25) Protesescu, L.; Yakunin, S.; Bodnarchuk, M. I.; Krieg, F.; Caputo, R.; Hendon, C. H.; Yang, R. X.; Walsh, A.; Kovalenko, M. V. Nanocrystals of Cesium Lead Halide Perovskites (CsPbX3, X = Cl, Br, and I): Novel Optoelectronic Materials Showing Bright Emission with Wide Color Gamut. *Nano Lett.* **2015**, *15*, 3692−3696.

(26) Saliba, M.; Correa-Baena, J.-P.; Grätzel, M.; Hagfeldt, A.; Abate, A. Perovskite Solar Cells: From the Atomic Level to Film Quality and Device Performance. *Angew. Chem., Int. Ed.* **2018**, *57*, 2554−2569.

(27) Evarestov, R. A.; Kotomin, E. A.; Senocrate, A.; Kremer, R. K.; Maier, J. First-principles comparative study of perfect and defective CsPbX3 (X = Br, I) crystals. *Phys. Chem. Chem. Phys.* **2020**, *22*, 3914−3920.

(28) Evarestov, R. A.; Senocrate, A.; Kotomin, E. A.; Maier, J. First-principles calculations of iodine-related point defects in CsPbI3. *Phys. Chem. Chem. Phys.* **2019**, *21*, 7841−7846.

(29) Qian, C.-X.; Deng, Z.-Y.; Yang, K.; Feng, J.; Wang, M.-Z.; Yang, Z.; Liu, S.; Feng, H.-J.; Feng, H.-J. Interface engineering of CsPbBr3/TiO2 heterostructure with enhanced optoelectronic properties for all-inorganic perovskite solar cells. *Appl. Phys. Lett.* **2018**, *112*, 093901.

(30) Yan, D.; Shi, T.; Zang, Z.; Zhou, T.; Liu, Z.; Zhang, Z.; Du, J.; Leng, Y.; Tang, X. Ultrastable CsPbBr 3 Perovskite Quantum Dot and Their Enhanced Amplified Spontaneous Emission by Surface Ligand Modification. *Small* **2019**, *15*, 1901173.

(31) Liu, F.; Zhang, Y.; Ding, C.; Toyoda, T.; Ogomi, Y.; Ripolles, T. S.; Hayase, S.; Minemoto, T.; Yoshino, K.; Dai, S.; et al. Ultrafast Electron Injection from Photoexcited Perovskite CsPbI3 QDs into TiO2 Nanoparticles with Injection Efficiency near 99%. *J. Phys. Chem. Lett.* **2018**, *9*, 294−297.

(32) Swarnkar, A.; Marshall, A. R.; Sanehira, E. M.; Chernomordik, B. D.; Moore, D. T.; Christians, J. A.; Chakrabarti, T.; Luther, J. M. Quantum dot-induced phase stabilization of α-CsPbI 3 perovskite for high-efficiency photovoltaics. *Science* **2016**, *354*, 92−95.

(33) Jena, A. K.; Kulkarni, A.; Miyasaka, T. Halide Perovskite Photovoltaics: Background, Status, and Future Prospects. *Chem. Rev.* **2019**, *119*, 3036−3103.

(34) Chang, X.; Fang, J.; Fan, Y.; Luo, T.; Su, H.; Zhang, Y.; Lu, J.; Tsetseris, L.; Anthopoulos, T. D.; Liu, S. F.; Zhao, K.; et al. Printable CsPbI3 Perovskite Solar Cells with PCE of 19% via an Additive Strategy. *Adv. Mater.* **2020**, *32*, No. e2001243.

(35) Li, X.; Tan, Y.; Lai, H.; Li, S.; Chen, Y.; Li, S.; Xu, P.; Yang, J. All-Inorganic CsPbBr3 Perovskite Solar Cells with 10.45% Efficiency by Evaporation-Assisted Deposition and Setting Intermediate Energy Levels. *ACS Appl. Mater. Interfaces* **2019**, *11*, 29746−29752.

(36) Ahn, N.; Son, D.-Y.; Jang, I.-H.; Kang, S. M.; Choi, M.; Park, N.-G. Highly Reproducible Perovskite Solar Cells with Average Efficiency of 18.3% and Best Efficiency of 19.7% Fabricated via Lewis

Base Adduct of Lead(II) Iodide. *J. Am. Chem. Soc.* **2015**, *137*, 8696−8699.

(37) Qin, P.; Tanaka, S.; Ito, S.; Tetreault, N.; Manabe, K.; Nishino, H.; Nazeeruddin, M. K.; Grätzel, M. Inorganic Hole Conductor-Based Lead Halide Perovskite Solar Cells with 12.4% Conversion Efficiency. *Nat. Commun.* **2014**, *5*, 3834.

(38) Nasti, G.; Abate, A. Tin Halide Perovskite (ASnX 3) Solar Cells: A Comprehensive Guide toward the Highest Power Conversion Efficiency. *Adv. Energy Mater.* **2020**, *10*, 1902467.

(39) Guijarro, N.; Yao, L.; Le Formal, F.; Wells, R. A.; Liu, Y.; Darwich, B. P.; Navratilova, L.; Cho, H. H.; Yum, J. H.; Sivula, K. Lead Halide Perovskite Quantum Dots To Enhance the Power Conversion Efficiency of Organic Solar Cells. *Angew. Chem.* **2019**, *131*, 12826−12834.

(40) Shamsi, J.; Urban, A. S.; Imran, M.; De Trizio, L.; Manna, L. Metal Halide Perovskite Nanocrystals: Synthesis, Post-Synthesis Modifications, and Their Optical Properties. *Chem. Rev.* **2019**, *119*, 3296−3348.

(41) Shockley, W.; Queisser, H. J. Detailed Balance Limit of Efficiency of p-n Junction Solar Cells. *J. Appl. Phys.* **1961**, *32*, 510−519.

(42) Rühle, S. Tabulated values of the Shockley-Queisser limit for single junction solar cells. *Sol. Energy* **2016**, *130*, 139−147.

(43) Hedin, L. New Method for Calculating the One-Particle Green's Function with Application to the Electron-Gas Problem. *Phys. Rev.* **1965**, *139*, A796−A823.

(44) Shishkin, M.; Kresse, G. Self-consistentGWcalculations for semiconductors and insulators. *Phys. Rev. B: Condens. Matter Mater. Phys.* **2007**, *75*, 235102.

(45) Zakharov, O.; Rubio, A.; Blase, X.; Cohen, M. L.; Louie, S. G. Quasiparticle Band Structures of Six II-VI Compounds: ZnS, ZnSe, ZnTe, CdS, CdSe, and CdTe. *Phys. Rev. B: Condens. Matter Mater. Phys.* **1994**, *50*, 10780−10787.

(46) Umari, P.; Mosconi, E.; De Angelis, F. Relativistic GW Calculations on CH3NH3PbI3 and CH3NH3SnI3 Perovskites for Solar Cell Applications. *Sci. Rep.* **2015**, *4*, 4467.

(47) Lang, L.; Zhang, Y.-Y.; Xu, P.; Chen, S.; Xiang, H. J.; Gong, X. G. Three-step approach for computing band offsets and its application to inorganicABX3halide perovskites. *Phys. Rev. B: Condens. Matter Mater. Phys.* **2015**, *92*, 075102.

(48) ten Brinck, S.; Infante, I. Surface Termination, Morphology, and Bright Photoluminescence of Cesium Lead Halide Perovskite Nanocrystals. *ACS Energy Lett.* **2016**, *1*, 1266−1272.

(49) Pascazio, R.; Zito, J.; Infante, I. An Overview of Computational Studies on Colloidal Semiconductor Nanocrystals. *Chim. Int. J. Chem.* **2021**, *75*, 427−434.

(50) Mosconi, E.; Amat, A.; Nazeeruddin, M. K.; Grätzel, M.; De Angelis, F. First-Principles Modeling of Mixed Halide Organometal Perovskites for Photovoltaic Applications. *J. Phys. Chem. C* **2013**, *117*, 13902−13913.

(51) Roiati, V.; Mosconi, E.; Listorti, A.; Colella, S.; Gigli, G.; De Angelis, F. Stark Effect in Perovskite/TiO2 Solar Cells: Evidence of Local Interfacial Order. *Nano Lett.* **2014**, *14*, 2168−2174.

(52) Castelli, I. E.; García-Lastra, J. M.; Thygesen, K. S.; Jacobsen, K. W. Bandgap Calculations and Trends of Organometal Halide Perovskites. *APL Mater.* **2014**, *2*, 081514.

(53) Pihosh, Y.; Turkevych, I.; Mawatari, K.; Uemura, J.; Kazoe, Y.; Kosar, S.; Makita, K.; Sugaya, T.; Matsui, T.; Fujita, D.; et al. Photocatalytic generation of hydrogen by core-shell WO3/BiVO4 nanorods with ultimate water splitting efficiency. *Sci. Rep.* **2015**, *5*, 11141.

(54) Wiktor, J.; Rothlisberger, U.; Pasquarello, A. Predictive Determination of Band Gaps of Inorganic Halide Perovskites. *J. Phys. Chem. Lett.* **2017**, *8*, 5507−5512.

(55) van Meer, R.; Gritsenko, O. V.; Baerends, E. J. Physical Meaning of Virtual Kohn-Sham Orbitals and Orbital Energies: An Ideal Basis for the Description of Molecular Excitations. *J. Chem. Theory Comput.* **2014**, *10*, 4432−4441.

(56) Amati, M.; Stoia, S.; Baerends, E. J. The Electron Affinity as the Highest Occupied Anion Orbital Energy with a Sufficiently Accurate Approximation of the Exact Kohn-Sham Potential. *J. Chem. Theory Comput.* **2020**, *16*, 443−452.

(57) Kronik, L.; Stein, T.; Refaely-Abramson, S.; Baer, R. Excitation Gaps of Finite-Sized Systems from Optimally Tuned Range-Separated Hybrid Functionals. *J. Chem. Theory Comput.* **2012**, *8*, 1515−1531.

(58) Baldini, E.; Chiodo, L.; Dominguez, A.; Palummo, M.; Moser, S.; Yazdi-Rizi, M.; Auböck, G.; Mallett, B. P. P.; Berger, H.; Magrez, A.; et al. Strongly Bound Excitons in Anatase TiO2 Single Crystals and Nanoparticles. *Nat. Commun.* **2017**, *8*, 13.

(59) Cipriano, L. A.; Di Liberto, G.; Tosoni, S.; Pacchioni, G. Band Gap in Magnetic Insulators from a Charge Transition Level Approach. *J. Chem. Theory Comput.* **2020**, *16*, 3786−3798.

(60) Chiodo, L.; García-Lastra, J. M.; Iacomino, A.; Ossicini, S.; Zhao, J.; Petek, H.; Rubio, A. Self-energy and excitonic effects in the electronic and optical properties ofTiO2crystalline phases. *Phys. Rev. B: Condens. Matter Mater. Phys.* **2010**, *82*, 045207.

(61) He, J.; Guo, M.; Long, R. Photoinduced Localized Hole Delays Nonradiative Electron-Hole Recombination in Cesium-Lead Halide Perovskites: A Time-Domain Ab Initio Analysis. *J. Phys. Chem. Lett.* **2018**, *9*, 3021−3028.

(62) Mladenović, M.; Vukmirović, N. Effects of Thermal Disorder on the Electronic Structure of Halide Perovskites: Insights from MD Simulations. *Phys. Chem. Chem. Phys.* **2018**, *20*, 25693−25700.

(63) Zhao, X.-G.; Wang, Z.; Malyi, O. I.; Zunger, A. Effect of Static Local Distortions vs. Dynamic Motions on the Stability and Band Gaps of Cubic Oxide and Halide Perovskites. *Mater. Today* **2021**, *49*, 107−122.

(64) Franchini, C. Hybrid Functionals Applied to Perovskites. *J. Phys.: Condens. Matter* **2014**, *26*, 253202.

(65) Jain, M.; Singh, A.; Basera, P.; Kumar, M.; Bhattacharya, S. Understanding the role of Sn substitution and Pb-□ in enhancing the optical properties and solar cell efficiency of CH(NH2)2Pb1−x−ySnx□yBr3. *J. Mater. Chem. C* **2020**, *8*, 10362−10368.

(66) Wang, X.; Wang, Q.; Chai, Z.; Wu, W. The thermal stability of FAPbBr3 nanocrystals from temperature-dependent photoluminescence and first-principles calculations. *RSC Adv.* **2020**, *10*, 44373−44381.

(67) Ghaithan, H. M.; Alahmed, Z. A.; Qaid, S. M. H.; Hezam, M.; Aldwayyan, A. S. Density Functional Study of Cubic, Tetragonal, and Orthorhombic CsPbBr3 Perovskite. *ACS Omega* **2020**, *5*, 7468−7480.

(68) Sa, R.; Liu, D.; Chen, Y.; Ying, S. Mixed-Cation Mixed-Metal Halide Perovskites for Photovoltaic Applications: A Theoretical Study. *ACS Omega* **2020**, *5*, 4347−4351.

(69) Jong, U.-G.; Yu, C.-J.; Kye, Y.-H.; Choe, Y.-G.; Hao, W.; Li, S. First-Principles Study on Structural, Electronic, and Optical Properties of Inorganic Ge-Based Halide Perovskites. *Inorg. Chem.* **2019**, *58*, 4134−4140.

(70) Kresse, G.; Furthmüller, J. Efficient iterative schemes forab initiototal-energy calculations using a plane-wave basis set. *Phys. Rev. B: Condens. Matter Mater. Phys.* **1996**, *54*, 11169−11186.

(71) Kresse, G.; Hafner, J. Ab initiomolecular dynamics for liquid metals. *Phys. Rev. B: Condens. Matter Mater. Phys.* **1993**, *47*, 558−561.

(72) Kresse, G.; Hafner, J. Ab initiomolecular-dynamics simulation of the liquid-metal-amorphous-semiconductor transition in germanium. *Phys. Rev. B: Condens. Matter Mater. Phys.* **1994**, *49*, 14251−14269.

(73) Blöchl, P. E. Projector Augmented-Wave Method. *Phys. Rev. B: Condens. Matter Mater. Phys.* **1994**, *50*, 17953−17979.

(74) Kresse, G.; Joubert, D. From Ultrasoft Pseudopotentials to the Projector Augmented-Wave Method. *Phys. Rev. B: Condens. Matter Mater. Phys.* **1999**, *59*, 1758−1775.

(75) Perdew, J. P.; Burke, K.; Ernzerhof, M. Generalized Gradient Approximation Made Simple. *Phys. Rev. Lett.* **1996**, *77*, 3865−3868.

(76) Heyd, J.; Scuseria, G. E.; Ernzerhof, M. Hybrid Functionals Based on a Screened Coulomb Potential. *J. Chem. Phys.* **2003**, *118*, 8207−8215.

https://doi.org/10.1021/acs.jpcc.1c09594

(77) Grimme, S.; Antony, J.; Ehrlich, S.; Krieg, H. A Consistent and Accurate Ab Initio Parametrization of Density Functional Dispersion Correction (DFT-D) for the 94 Elements H-Pu. *J. Chem. Phys.* **2010**, *132*, 154104.

(78) Steiner, S.; Khmelevskyi, S.; Marsmann, M.; Kresse, G. Calculation of the magnetic anisotropy with projected-augmented-wave methodology and the case study of disorderedFe1−xCoxalloys. *Phys. Rev. B* **2016**, *93*, 224425.

(79) Körbel, S.; Marques, M. A. L.; Botti, S. Stability and Electronic Properties of New Inorganic Perovskites from High-Throughput Ab Initio Calculations. *J. Mater. Chem. C* **2016**, *4*, 3157−3167.

(80) Lee, J.-H.; Bristowe, N. C.; Lee, J. H.; Lee, S.-H.; Bristowe, P. D.; Cheetham, A. K.; Jang, H. M. Resolving the Physical Origin of Octahedral Tilting in Halide Perovskites. *Chem. Mater.* **2016**, *28*, 4259−4266.

(81) Frost, J. M.; Walsh, A. What Is Moving in Hybrid Halide Perovskite Solar Cells? *Acc. Chem. Res.* **2016**, *49*, 528−535.

(82) Gerosa, M.; Bottani, C. E.; Caramella, L.; Onida, G.; Di Valentin, C.; Pacchioni, G. Electronic structure and phase stability of oxide semiconductors: Performance of dielectric-dependent hybrid functional DFT, benchmarked againstGWband structure calculations and experiments. *Phys. Rev. B: Condens. Matter Mater. Phys.* **2015**, *91*, 1−15.

(83) Alkauskas, A.; Broqvist, P.; Pasquarello, A. Defect Levels through Hybrid Density Functionals: Insights and Applications. *Phys. Status Solidi* **2011**, *248*, 775−789.

(84) Skone, J. H.; Govoni, M.; Galli, G. Self-Consistent Hybrid Functional for Condensed Systems. *Phys. Rev. B: Condens. Matter Mater. Phys.* **2014**, *89*, 195112.

(85) Gerosa, M.; Bottani, C. E.; Di Valentin, C.; Onida, G.; Pacchioni, G. Accuracy of dielectric-dependent hybrid functionals in the prediction of optoelectronic properties of metal oxide semiconductors: a comprehensive comparison with many-bodyGWand experiments. *J. Phys.: Condens. Matter* **2018**, *30*, 044003.

(86) Chen, W.; Pasquarello, A. Correspondence of Defect Energy Levels in Hybrid Density Functional Theory and Many-Body Perturbation Theory. *Phys. Rev. B: Condens. Matter Mater. Phys.* **2013**, *88*, 115104.

(87) Das, T.; Di Liberto, G.; Tosoni, S.; Pacchioni, G. Band Gap of 3D Metal Oxides and Quasi-2D Materials from Hybrid Density Functional Theory: Are Dielectric-Dependent Functionals Superior? *J. Chem. Theory Comput.* **2019**, *15*, 6294−6312.

(88) Heidrich, K.; Schäfer, W.; Schreiber, M.; Söchtig, J.; Trendel, G.; Treusch, J.; Grandke, T.; Stolz, H. J. Electronic structure, photoemission spectra, and vacuum-ultraviolet optical spectra of CsPbCl3and CsPbBr3. *Phys. Rev. B: Condens. Matter Mater. Phys.* **1981**, *24*, 5642−5649.

(89) Jang, D. M.; Kim, D. H.; Park, K.; Park, J.; Lee, J. W.; Song, J. K. Ultrasound Synthesis of Lead Halide Perovskite Nanocrystals. *J. Mater. Chem. C* **2016**, *4*, 10625−10629.

(90) Rao, Z.; Liang, W.; Huang, H.; Ge, J.; Wang, W.; Pan, S. High sensitivity and rapid response ultraviolet photodetector of a tetragonal CsPbCl3 perovskite single crystal. *Opt. Mater. Express* **2020**, *10*, 1374.

(91) Kulbak, M.; Cahen, D.; Hodes, G. How Important Is the Organic Part of Lead Halide Perovskite Photovoltaic Cells? Efficient CsPbBr3 Cells. *J. Phys. Chem. Lett.* **2015**, *6*, 2452−2456.

(92) Stoumpos, C. C.; Malliakas, C. D.; Peters, J. A.; Liu, Z.; Sebastian, M.; Im, J.; Chasapis, T. C.; Wibowo, A. C.; Chung, D. Y.; Freeman, A. J.; et al. Crystal Growth of the Perovskite Semiconductor CsPbBr3: A New Material for High-Energy Radiation Detection. *Cryst. Growth Des.* **2013**, *13*, 2722−2727.

(93) Sebastian, M.; Peters, J. A.; Stoumpos, C. C.; Im, J.; Kostina, S. S.; Liu, Z.; Kanatzidis, M. G.; Freeman, A. J.; Wessels, B. W. Excitonic emissions and above-band-gap luminescence in the single-crystal perovskite semiconductorsCsPbBr3andCsPbCl3. *Phys. Rev. B: Condens. Matter Mater. Phys.* **2015**, *92*, 235210.

(94) Nasi, L.; Calestani, D.; Mezzadri, F.; Mariano, F.; Listorti, A.; Ferro, P.; Mazzeo, M.; Mosca, R. All-Inorganic CsPbBr3 Perovskite Films Prepared by Single Source Thermal Ablation. *Front. Chem.* **2020**, *8*, 313.

(95) Chen, C.; Wu, D.; Yuan, M.; Yu, C.; Zhang, J.; Li, C.; Duan, Y. Spectroscopic ellipsometry study of CsPbBr3 perovskite thin films prepared by vacuum evaporation. *J. Phys. D: Appl. Phys.* **2021**, *54*, 224002.

(96) Ghaithan, H. M.; Qaid, S. M. H.; Alahmed, Z. A.; Hezam, M.; Lyras, A.; Amer, M.; Aldwayyan, A. S. Anion Substitution Effects on the Structural, Electronic, and Optical Properties of Inorganic CsPb(I1-xBrx)3 and CsPb(Br1-xClx)3 Perovskites: Theoretical and Experimental Approaches. *J. Phys. Chem. C* **2021**, *125*, 886−897.

(97) Whitcher, T. J.; Gomes, L. C.; Zhao, D.; Bosman, M.; Chi, X.; Wang, Y.; Carvalho, A.; Hui, H. K.; Chang, Q.; Breese, M. B. H.; et al. Dual Phases of Crystalline and Electronic Structures in the Nanocrystalline Perovskite CsPbBr3. *NPG Asia Mater.* **2019**, *11*, 70.

(98) Hoffman, J. B.; Schleper, A. L.; Kamat, P. V. Transformation of Sintered CsPbBr3 Nanocrystals to Cubic CsPbI3 and Gradient CsPbBrxI3-x through Halide Exchange. *J. Am. Chem. Soc.* **2016**, *138*, 8603−8611.

(99) Eperon, G. E.; Stranks, S. D.; Menelaou, C.; Johnston, M. B.; Herz, L. M.; Snaith, H. J. Formamidinium Lead Trihalide: A Broadly Tunable Perovskite for Efficient Planar Heterojunction Solar Cells. *Energy Environ. Sci.* **2014**, *7*, 982.

(100) Yang, Z.; Surrente, A.; Galkowski, K.; Miyata, A.; Portugall, O.; Sutton, R. J.; Haghighirad, A. A.; Snaith, H. J.; Maude, D. K.; Plochocka, P.; et al. Impact of the Halide Cage on the Electronic Properties of Fully Inorganic Cesium Lead Halide Perovskites. *ACS Energy Lett.* **2017**, *2*, 1621−1627.

(101) Zhao, B.; Jin, S.-F.; Huang, S.; Liu, N.; Ma, J.-Y.; Xue, D.-J.; Han, Q.; Ding, J.; Ge, Q.-Q.; Feng, Y.; et al. Thermodynamically Stable Orthorhombic γ-CsPbI3 Thin Films for High-Performance Photovoltaics. *J. Am. Chem. Soc.* **2018**, *140*, 11716−11725.

(102) Straus, D. B.; Guo, S.; Cava, R. J. Kinetically Stable Single Crystals of Perovskite-Phase CsPbI3. *J. Am. Chem. Soc.* **2019**, *141*, 11435−11439.

(103) Pawar, V.; Kumar, M.; Jha, P. A.; Gupta, S. K.; Sinha, A. S. K.; Jha, P. K.; Singh, P. Ambient Atmospheric Temperature Processed Lead Halide Perovskites. *J. Therm. Anal. Calorim.* **2020**, *139*, 3073−3078.

(104) Voloshinovskii, A. S.; Myagkota, S. V.; Pidzyrailo, N. S.; Tokarivskii, M. V. Luminescence and Structural Transformations of CsSnCl3 Crystals. *J. Appl. Spectrosc.* **1994**, *60*, 226−228.

(105) Peedikakkandy, L.; Bhargava, P. Composition Dependent Optical, Structural and Photoluminescence Characteristics of Cesium Tin Halide Perovskites. *RSC Adv.* **2016**, *6*, 19857−19860.

(106) Coduri, M.; Strobel, T. A.; Szafrański, M.; Katrusiak, A.; Mahata, A.; Cova, F.; Bonomi, S.; Mosconi, E.; De Angelis, F.; Malavasi, L. Band Gap Engineering in MASnBr3 and CsSnBr3 Perovskites: Mechanistic Insights through the Application of Pressure. *J. Phys. Chem. Lett.* **2019**, *10*, 7398−7405.

(107) Fang, D.; Tong, Y.; Xu, F.; Mi, B.; Cao, D.; Gao, Z. Preparation of CsSnBr3 Perovskite Film and Its All-Inorganic Solar Cells with Planar Heterojunction. *J. Solid State Chem.* **2021**, *294*, 121902.

(108) Li, B.; Long, R.; Xia, Y.; Mi, Q. All-Inorganic Perovskite CsSnBr 3 as a Thermally Stable, Free-Carrier Semiconductor. *Angew. Chem., Int. Ed.* **2018**, *57*, 13154−13158.

(109) Yu, C.; Chen, Z.; Wang, J. J.; Pfenninger, W.; Vockic, N.; Kenney, J. T.; Shum, K. Temperature dependence of the band gap of perovskite semiconductor compound CsSnI3. *J. Appl. Phys.* **2011**, *110*, 063526.

(110) Chen, Z.; Yu, C.; Shum, K.; Wang, J. J.; Pfenninger, W.; Vockic, N.; Midgley, J.; Kenney, J. T. Photoluminescence Study of Polycrystalline CsSnI3 Thin Films: Determination of Exciton Binding Energy. *J. Lumin.* **2012**, *132*, 345−349.

(111) Chung, I.; Song, J.-H.; Im, J.; Androulakis, J.; Malliakas, C. D.; Li, H.; Freeman, A. J.; Kenney, J. T.; Kanatzidis, M. G. CsSnI3: Semiconductor or Metal? High Electrical Conductivity and Strong Near-Infrared Photoluminescence from a Single Material. High Hole

Mobility and Phase-Transitions. *J. Am. Chem. Soc.* **2012**, *134*, 8579−8587.

(112) Ye, T.; Wang, X.; Wang, K.; Ma, S.; Yang, D.; Hou, Y.; Yoon, J.; Wang, K.; Priya, S. Localized Electron Density Engineering for Stabilized B-γ CsSnI3-Based Perovskite Solar Cells with Efficiencies >10%. *ACS Energy Lett.* **2021**, *6*, 1480−1489.

(113) Tang, L.-C.; Chang, Y.-C.; Huang, J.-Y.; Lee, M.-H.; Chang, C.-S. First Principles Calculations of Linear and Second-Order Optical Responses in Rhombohedrally Distorted Perovskite Ternary Halides, CsGeX3(X = Cl, Br, and I). *Jpn. J. Appl. Phys.* **2009**, *48*, 112402.

(114) Chen, L.-J. Synthesis and Optical Properties of Lead-Free Cesium Germanium Halide Perovskite Quantum Rods. *RSC Adv.* **2018**, *8*, 18396−18399.

(115) Lin, Z.-G.; Tang, L.-C.; Chou, C.-P. Characterization and Properties of Infrared NLO Crystals: AGeX3 (A=Rb, Cs; X=Cl, Br). *J. Cryst. Growth* **2008**, *310*, 3224−3229.

(116) Krishnamoorthy, T.; Ding, H.; Yan, C.; Leong, W. L.; Baikie, T.; Zhang, Z.; Sherburne, M.; Li, S.; Asta, M.; Mathews, N.; et al. Lead-Free Germanium Iodide Perovskite Materials for Photovoltaic Applications. *J. Mater. Chem. A* **2015**, *3*, 23829−23832.

(117) Leguy, A. M. A.; Azarhoosh, P.; Alonso, M. I.; Campoy-Quiles, M.; Weber, O. J.; Yao, J.; Bryant, D.; Weller, M. T.; Nelson, J.; Walsh, A.; et al. Experimental and Theoretical Optical Properties of Methylammonium Lead Halide Perovskites. *Nanoscale* **2016**, *8*, 6317−6327.

(118) Glaser, T.; Müller, C.; Sendner, M.; Krekeler, C.; Semonin, O. E.; Hull, T. D.; Yaffe, O.; Owen, J. S.; Kowalsky, W.; Pucci, A.; et al. Infrared Spectroscopic Study of Vibrational Modes in Methylammonium Lead Halide Perovskites. *J. Phys. Chem. Lett.* **2015**, *6*, 2913−2918.

(119) Maculan, G.; Sheikh, A. D.; Abdelhady, A. L.; Saidaminov, M. I.; Haque, M. A.; Murali, B.; Alarousu, E.; Mohammed, O. F.; Wu, T.; Bakr, O. M. CH3NH3PbCl3 Single Crystals: Inverse Temperature Crystallization and Visible-Blind UV-Photodetector. *J. Phys. Chem. Lett.* **2015**, *6*, 3781−3786.

(120) Nandi, P.; Giri, C.; Swain, D.; Manju, U.; Topwal, D. Room temperature growth of CH3NH3PbCl3 single crystals by solvent evaporation method. *CrystEngComm* **2019**, *21*, 656−661.

(121) Sektiono, M. W. A.; Permatasari, F. A.; Aimon, A. H.; Iskandar, F. Rapid growth of the CH3NH3PbCl3 single crystal by microwave irradiation. *RSC Adv.* **2021**, *11*, 1360−1366.

(122) Tang, M.-C.; Dang, H. X.; Lee, S.; Barrit, D.; Munir, R.; Wang, K.; Li, R.; Smilgies, D.-M.; De Wolf, S.; Kim, D.-Y.; et al. Wide and Tunable Bandgap MAPbBr 3− x Cl x Hybrid Perovskites with Enhanced Phase Stability: In Situ Investigation and Photovoltaic Devices. *Sol. RRL* **2021**, *5*, 2000718.

(123) Rigter, S. A.; Quinn, X. L.; Kumar, R. E.; Fenning, D. P.; Massonnet, P.; Ellis, S. R.; Heeren, R. M. A.; Svane, K. L.; Walsh, A.; Garnett, E. C. Passivation Properties and Formation Mechanism of Amorphous Halide Perovskite Thin Films. *Adv. Funct. Mater.* **2021**, *31*, 2010330.

(124) Baikie, T.; Barrow, N. S.; Fang, Y.; Keenan, P. J.; Slater, P. R.; Piltz, R. O.; Gutmann, M.; Mhaisalkar, S. G.; White, T. J. A combined single crystal neutron/X-ray diffraction and solid-state nuclear magnetic resonance study of the hybrid perovskites CH3NH3PbX3 (X = I, Br and Cl). *J. Mater. Chem. A* **2015**, *3*, 9298−9307.

(125) Mannino, G.; Deretzis, I.; Smecca, E.; La Magna, A.; Alberti, A.; Ceratti, D.; Cahen, D. Temperature-Dependent Optical Band Gap in CsPbBr3, MAPbBr3, and FAPbBr3 Single Crystals. *J. Phys. Chem. Lett.* **2020**, *11*, 2490−2496.

(126) Galkowski, K.; Mitioglu, A.; Miyata, A.; Plochocka, P.; Portugall, O.; Eperon, G. E.; Wang, J. T.-W.; Stergiopoulos, T.; Stranks, S. D.; Snaith, H. J.; et al. Determination of the Exciton Binding Energy and Effective Masses for Methylammonium and Formamidinium Lead Tri-Halide Perovskite Semiconductors. *Energy Environ. Sci.* **2016**, *9*, 962−970.

(127) Chi, X.; Leng, K.; Wu, B.; Shi, D.; Choy, Y.; Chen, Z.; Chen, Z.; Yu, X.; Yang, P.; Xu, Q.-H.; et al. Elucidating Surface and Bulk Emission in 3D Hybrid Organic-Inorganic Lead Bromide Perovskites. *Adv. Opt. Mater.* **2018**, *6*, 1800470.

(128) Quarti, C.; Mosconi, E.; Ball, J. M.; D'Innocenzo, V.; Tao, C.; Pathak, S.; Snaith, H. J.; Petrozza, A.; De Angelis, F. Structural and Optical Properties of Methylammonium Lead Iodide across the Tetragonal to Cubic Phase Transition: Implications for Perovskite Solar Cells. *Energy Environ. Sci.* **2016**, *9*, 155−163.

(129) Hao, F.; Stoumpos, C. C.; Chang, R. P. H.; Kanatzidis, M. G. Anomalous Band Gap Behavior in Mixed Sn and Pb Perovskites Enables Broadening of Absorption Spectrum in Solar Cells. *J. Am. Chem. Soc.* **2014**, *136*, 8094−8099.

(130) Jiang, S.; Fang, Y.; Li, R.; Xiao, H.; Crowley, J.; Wang, C.; White, T. J.; Goddard, W. A.; Wang, Z.; Baikie, T.; et al. Pressure-Dependent Polymorphism and Band-Gap Tuning of Methylammonium Lead Iodide Perovskite. *Angew. Chem.* **2016**, *128*, 6650−6654.

(131) Zeng, L.; Chen, Z.; Qiu, S.; Hu, J.; Li, C.; Liu, X.; Liang, G.; Brabec, C. J.; Mai, Y.; Guo, F. 2D-3D heterostructure enables scalable coating of efficient low-bandgap Sn-Pb mixed perovskite solar cells. *Nano Energy* **2019**, *66*, 104099.

(132) Xu, Z.; Li, H.; Zhao, H.; Fu, Q.; Tao, H.; Wang, S.; Ma, Z.; Ding, J.; Ma, Y.; Han, Y. Optimizing optoelectronic performances by controlling halide compositions of MAPb(ClxI1−x)3 single crystals. *CrystEngComm* **2019**, *21*, 4169−4174.

(133) Ishihara, T. Optical Properties of PbI-Based Perovskite Structures. *J. Lumin.* **1994**, *60*−*61*, 269−274.

(134) Baikie, T.; Fang, Y.; Kadro, J. M.; Schreyer, M.; Wei, F.; Mhaisalkar, S. G.; Graetzel, M.; White, T. J. Synthesis and Crystal Chemistry of the Hybrid Perovskite (CH3NH3)PbI3 for Solid-State Sensitised Solar Cell Applications. *J. Mater. Chem. A* **2013**, *1*, 5628.

(135) Cheng, F. J.; Hu, S. Y.; Chen, L. Y.; Lee, Y. C.; Yin, G. Z.; Tiong, K. K.; Shen, J. L. Time-Resolved Photoluminescence Studies on Localization Effects in Orthorhombic Phase of CH3NH3PbI3 Perovskite Thin Film. *J. Lumin.* **2018**, *197*, 248−251.

(136) Chiarella, F.; Zappettini, A.; Licci, F.; Borriello, I.; Cantele, G.; Ninno, D.; Cassinese, A.; Vaglio, R. Combined experimental and theoretical investigation of optical, structural, and electronic properties ofCH3NH3SnX3thin films(X=Cl,Br). *Phys. Rev. B: Condens. Matter Mater. Phys.* **2008**, *77*, 045129.

(137) Pandech, N.; Kongnok, T.; Palakawong, N.; Limpijumnong, S.; Lambrecht, W. R. L.; Jungthawan, S. Effects of the van der Waals Interactions on Structural and Electronic Properties of CH3NH3-(Pb,Sn)(I,Br,Cl)3 Halide Perovskites. *ACS Omega* **2020**, *5*, 25723−25732.

(138) Jung, M.-C.; Raga, S. R.; Qi, Y. Properties and Solar Cell Applications of Pb-Free Perovskite Films Formed by Vapor Deposition. *RSC Adv.* **2016**, *6*, 2819−2825.

(139) Stoumpos, C. C.; Malliakas, C. D.; Kanatzidis, M. G. Semiconducting Tin and Lead Iodide Perovskites with Organic Cations: Phase Transitions, High Mobilities, and Near-Infrared Photoluminescent Properties. *Inorg. Chem.* **2013**, *52*, 9019−9038.

(140) Zhao, Y.; Wei, J.; Li, H.; Yan, Y.; Zhou, W.; Yu, D.; Zhao, Q. A Polymer Scaffold for Self-Healing Perovskite Solar Cells. *Nat. Commun.* **2016**, *7*, 10228.

(141) Noel, N. K.; Stranks, S. D.; Abate, A.; Wehrenfennig, C.; Guarnera, S.; Haghighirad, A.-A.; Sadhanala, A.; Eperon, G. E.; Pathak, S. K.; Johnston, M. B.; et al. Lead-free organic-inorganic tin halide perovskites for photovoltaic applications. *Energy Environ. Sci.* **2014**, *7*, 3061−3068.

(142) Shi, Z.; Guo, J.; Chen, Y.; Li, Q.; Pan, Y.; Zhang, H.; Xia, Y.; Huang, W. Lead-Free Organic-Inorganic Hybrid Perovskites for Photovoltaic Applications: Recent Advances and Perspectives. *Adv. Mater.* **2017**, *29*, 1605005.

(143) Dang, Y.; Zhou, Y.; Liu, X.; Ju, D.; Xia, S.; Xia, H.; Tao, X. Formation of Hybrid Perovskite Tin Iodide Single Crystals by Top-Seeded Solution Growth. *Angew. Chem., Int. Ed.* **2016**, *55*, 3447−3450.

(144) Ogomi, Y.; Morita, A.; Tsukamoto, S.; Saitho, T.; Fujikawa, N.; Shen, Q.; Toyoda, T.; Yoshino, K.; Pandey, S. S.; Ma, T.; et al.

CH3NH3SnxPb(1-x)I3 Perovskite Solar Cells Covering up to 1060 nm. *J. Phys. Chem. Lett.* **2014**, *5*, 1004−1011.

(145) Parrott, E. S.; Milot, R. L.; Stergiopoulos, T.; Snaith, H. J.; Johnston, M. B.; Herz, L. M. Effect of Structural Phase Transition on Charge-Carrier Lifetimes and Defects in CH3NH3SnI3 Perovskite. *J. Phys. Chem. Lett.* **2016**, *7*, 1321−1326.

(146) Chang, X.; Marongiu, D.; Sarritzu, V.; Sestu, N.; Wang, Q.; Lai, S.; Mattoni, A.; Filippetti, A.; Congiu, F.; Lehmann, A. G.; et al. Layered Germanium Hybrid Perovskite Bromides: Insights from Experiments and First-Principles Calculations. *Adv. Funct. Mater.* **2019**, *29*, 1903528.

(147) Stoumpos, C. C.; Frazer, L.; Clark, D. J.; Kim, Y. S.; Rhim, S. H.; Freeman, A. J.; Ketterson, J. B.; Jang, J. I.; Kanatzidis, M. G. Hybrid Germanium Iodide Perovskite Semiconductors: Active Lone Pairs, Structural Distortions, Direct and Indirect Energy Gaps, and Strong Nonlinear Optical Properties. *J. Am. Chem. Soc.* **2015**, *137*, 6804−6819.

(148) Nagane, S.; Ghosh, D.; Hoye, R. L. Z.; Zhao, B.; Ahmad, S.; Walker, A. B.; Islam, M. S.; Ogale, S.; Sadhanala, A. Lead-Free Perovskite Semiconductors Based on Germanium-Tin Solid Solutions: Structural and Optoelectronic Properties. *J. Phys. Chem. C* **2018**, *122*, 5940−5947.

(149) Cheng, M.; Li, G.; Li, H.; Xu, E.; Li, D.; Wang, H.; Wu, F.; Zhong, H.; Jiang, Y. Full Visible Waveband Tunable Formamidinium Halides Hybrid Perovskite QDs via Anion-Exchange Route and Their High Luminous Efficiency LEDs. *J. Alloys Compd.* **2019**, *791*, 814−821.

(150) Levchuk, I.; Osvet, A.; Tang, X.; Brandl, M.; Perea, J. D.; Hoegl, F.; Matt, G. J.; Hock, R.; Batentschuk, M.; Brabec, C. J. Brightly Luminescent and Color-Tunable Formamidinium Lead Halide Perovskite FAPbX3 (X = Cl, Br, I) Colloidal Nanocrystals. *Nano Lett.* **2017**, *17*, 2765−2770.

(151) Diroll, B. T.; Mannodi-Kanakkithodi, A.; Chan, M. K. Y.; Schaller, R. D. Spectroscopic Comparison of Thermal Transport at Organic-Inorganic and Organic-Hybrid Interfaces Using CsPbBr3 and FAPbBr3 (FA = Formamidinium) Perovskite Nanocrystals. *Nano Lett.* **2019**, *19*, 8155−8160.

(152) Wang, L.; Wang, K.; Zou, B. Pressure-Induced Structural and Optical Properties of Organometal Halide Perovskite-Based Formamidinium Lead Bromide. *J. Phys. Chem. Lett.* **2016**, *7*, 2556−2562.

(153) Zhumekenov, A. A.; Saidaminov, M. I.; Haque, M. A.; Alarousu, E.; Sarmah, S. P.; Murali, B.; Dursun, I.; Miao, X.-H.; Abdelhady, A. L.; Wu, T.; et al. Formamidinium Lead Halide Perovskite Crystals with Unprecedented Long Carrier Dynamics and Diffusion Length. *ACS Energy Lett.* **2016**, *1*, 32−37.

(154) Protesescu, L.; Yakunin, S.; Kumar, S.; Bär, J.; Bertolotti, F.; Masciocchi, N.; Guagliardi, A.; Grotevent, M.; Shorubalko, I.; Bodnarchuk, M. I.; et al. Dismantling the "Red Wall" of Colloidal Perovskites: Highly Luminescent Formamidinium and Formamidinium−Cesium Lead Iodide Nanocrystals. *ACS Nano* **2017**, *11*, 3119−3134.

(155) Whitcher, T. J.; Zhu, J.-X.; Chi, X.; Hu, H.; Zhao, D.; Asmara, T. C.; Yu, X.; Breese, M. B. H.; Castro Neto, A. H.; Lam, Y. M.; et al. Importance of Electronic Correlations and Unusual Excitonic Effects in Formamidinium Lead Halide Perovskites. *Phys. Rev. X* **2018**, *8*, 021034.

(156) Yamada, K.; Fujise, K.; Hino, S.; Yamane, Y.; Nakagama, T. Characterization of Sn(II)-based Perovskites by XRD, DTA, NQR and119Sn NMR for Photovoltaic Applications. *Chem. Lett.* **2019**, *48*, 749−752.

(157) Coduri, M.; Shiell, T. B.; Strobel, T. A.; Mahata, A.; Cova, F.; Mosconi, E.; De Angelis, F.; Malavasi, L. Origin of Pressure-Induced Band Gap Tuning in Tin Halide Perovskites. *Mater. Adv.* **2020**, *1*, 2840−2845.

(158) Sekimoto, T.; Suzuka, M.; Yokoyama, T.; Miyamoto, Y.; Uchida, R.; Hiraoka, M.; Kawano, K.; Sekiguchi, T.; Kaneko, Y. Inverse Temperature Crystallization of Formamidinium Tin Iodide: Indirect Transition State and Restriction of Cation Motion. *Cryst. Growth Des.* **2020**, *20*, 874−883.

(159) Lee, J.-W.; Seol, D.-J.; Cho, A.-N.; Park, N.-G. High-Efficiency Perovskite Solar Cells Based on the Black Polymorph of HC(NH2)-2PbI3. *Adv. Mater.* **2014**, *26*, 4991−4998.

(160) Kahmann, S.; Nazarenko, O.; Shao, S.; Hordiichuk, O.; Kepenekian, M.; Even, J.; Kovalenko, M. V.; Blake, G. R.; Loi, M. A. Negative Thermal Quenching in FASnI3 Perovskite Single Crystals and Thin Films. *ACS Energy Lett.* **2020**, *5*, 2512−2519.

(161) Lee, S. J.; Shin, S. S.; Kim, Y. C.; Kim, D.; Ahn, T. K.; Noh, J. H.; Seo, J.; Seok, S. I. Fabrication of Efficient Formamidinium Tin Iodide Perovskite Solar Cells through SnF2-Pyrazine Complex. *J. Am. Chem. Soc.* **2016**, *138*, 3974−3977.

(162) Koh, T. M.; Krishnamoorthy, T.; Yantara, N.; Shi, C.; Leong, W. L.; Boix, P. P.; Grimsdale, A. C.; Mhaisalkar, S. G.; Mathews, N. Formamidinium tin-based perovskite with low Eg for photovoltaic applications. *J. Mater. Chem. A* **2015**, *3*, 14996−15000.

(163) Jokar, E.; Chien, C.-H.; Tsai, C.-M.; Fathi, A.; Diau, E. W.-G. Robust Tin-Based Perovskite Solar Cells with Hybrid Organic Cations to Attain Efficiency Approaching 10%. *Adv. Mater.* **2019**, *31*, 1804835.

(164) Xue, J.; Yang, D.; Cai, B.; Xu, X.; Wang, J.; Ma, H.; Yu, X.; Yuan, G.; Zou, Y.; Song, J.; et al. Photon-Induced Reversible Phase Transition in CsPbBr 3 Perovskite. *Adv. Funct. Mater.* **2019**, *29*, 1807922.

(165) Yamada, Y.; Nakamura, T.; Endo, M.; Wakamiya, A.; Kanemitsu, Y. Near-band-edge optical responses of solution-processed organic-inorganic hybrid perovskite CH3NH3PbI3on mesoporous TiO2electrodes. *Appl. Phys. Express* **2014**, *7*, 032302.

(166) Wehrenfennig, C.; Liu, M.; Snaith, H. J.; Johnston, M. B.; Herz, L. M. Homogeneous Emission Line Broadening in the Organo Lead Halide Perovskite CH3NH3PbI3-xClx. *J. Phys. Chem. Lett.* **2014**, *5*, 1300−1306.

(167) Fang, H.-H.; Raissa, R.; Abdu-Aguye, M.; Adjokatse, S.; Blake, G. R.; Even, J.; Loi, M. A. Photophysics of Organic-Inorganic Hybrid Lead Iodide Perovskite Single Crystals. *Adv. Funct. Mater.* **2015**, *25*, 2378−2385.

(168) Kong, W.; Ye, Z.; Qi, Z.; Zhang, B.; Wang, M.; Rahimi-Iman, A.; Wu, H. Characterization of an abnormal photoluminescence behavior upon crystal-phase transition of perovskite CH3NH3PbI3. *Phys. Chem. Chem. Phys.* **2015**, *17*, 16405−16411.

(169) Im, J.; Stoumpos, C. C.; Jin, H.; Freeman, A. J.; Kanatzidis, M. G. Antagonism between Spin-Orbit Coupling and Steric Effects Causes Anomalous Band Gap Evolution in the Perovskite Photovoltaic Materials CH3NH3Sn1-xPbxI3. *J. Phys. Chem. Lett.* **2015**, *6*, 3503−3509.

(170) Amat, A.; Mosconi, E.; Ronca, E.; Quarti, C.; Umari, P.; Nazeeruddin, M. K.; Grätzel, M.; De Angelis, F. Cation-Induced Band-Gap Tuning in Organohalide Perovskites: Interplay of Spin-Orbit Coupling and Octahedra Tilting. *Nano Lett.* **2014**, *14*, 3608−3616.

(171) Even, J.; Pedesseau, L.; Jancu, J.-M.; Katan, C. Importance of Spin-Orbit Coupling in Hybrid Organic/Inorganic Perovskites for Photovoltaic Applications. *J. Phys. Chem. Lett.* **2013**, *4*, 2999−3005.

(172) Jolliffe, I. T. *Principal Component Analysis*; Springer Series in Statistics; Springer-Verlag: New York, 2002.

(173) Gavezzotti, A.; Presti, L. L. Building Blocks of Crystal Engineering: A Large-Database Study of the Intermolecular Approach between C-H Donor Groups and O, N, Cl, or F Acceptors in Organic Crystals. *Cryst. Growth Des.* **2016**, *16*, 2952−2962.

(174) Colombo, V.; Presti, L. L.; Gavezzotti, A. Two-Component Organic Crystals without Hydrogen Bonding: Structure and Intermolecular Interactions in Bimolecular Stacking. *CrystEngComm* **2017**, *19*, 2413−2423.

(175) R Core Team (2014). R: A Language and Environment for Statistical Computing. *R Foundation for Statistical Computing*, Vienna, Austria, 2013; Vol. *3* (1), p 201. Http://Www.R-Project.Org/.

(176) Mittal, M.; Jana, A.; Sarkar, S.; Mahadevan, P.; Sapra, S. Size of the Organic Cation Tunes the Band Gap of Colloidal Organolead Bromide Perovskite Nanocrystals. *J. Phys. Chem. Lett.* **2016**, *7*, 3270−3277.

(177) Belghachi, A. Theoretical Calculation of the Efficiency Limit for Solar Cells. In *Solar Cells—New Approaches and Reviews*; InTech, 2015.